PCCP

ROYAL SOCIETY OF CHEMISTRY

PAPER

View Article Online
View Journal | View Issue

Cite this: *Phys. Chem. Chem. Phys.*, 2025, **27**, 7336

Delineating the tryptophan–galactosylamine conjugate mediated structural distortions in $A\beta_{42}$ protofibrils†

Arushi Dabas and Bhupesh Goyal *

Amyloid-β (Aβ) fibrillation into neurotoxic soluble oligomers and mature fibrils is mainly responsible for the etiology of Alzheimer's disease (AD). A recent study revealed 61% disaggregation of the pre-formed $A\beta_{42}$ fibrils upon incubating with a highly soluble tryptophan–galactosylamine conjugate, WGalNAc. WGalNAc displayed no toxicity and increased the viability of SH-SY5Y cells up to 62.9 ± 2% with an EC_{50} value of 2.3 μM against $A\beta_{42}$ pre-formed fibrils. However, the key interactions and disruptive mechanism of WGalNAc against Aβ fibrils remain elusive. Thus, mechanistic insights into the disruptive potential of WGalNAc against $A\beta_{42}$ protofibrils (PDB: 5OQV) were examined using molecular dynamics (MD) simulations. The molecular docking depicted a favourable binding energy (−6.60 kcal mol^{-1}) and interaction of WGalNAc with the central hydrophobic core (CHC) region of chain A of the 5OQV protofibril. The MD simulations depicted that WGalNAc disrupted the contacts among Ala2, Phe4, Leu34, and Val36 in the hydrophobic core 1 of the 5OQV protofibril responsible for maintaining the stability of the LS-shaped 5OQV protofibril. WGalNAc binds favourably to the 5OQV protofibril ($\Delta G_{binding}$ = −21.76 ± 2.40 kcal mol^{-1}) with a significant contribution from the van der Waals interaction term. Notably, the binding affinity between the neighbouring chains of the 5OQV protofibril was significantly reduced from −134.31 ± 11.12 to −121.88 ± 1.95 kcal mol^{-1} upon the incorporation of WGalNAc, which is consistent with the ThT kinetic results that revealed disaggregation of the pre-formed $A\beta_{42}$ fibrils upon incubating with WGalNAc. The *in silico* ADMET properties of WGalNAc showed its ability as a promising therapeutic candidate due to its blood–brain barrier (BBB) permeability, extended half-life, and non-toxic profile. The MD simulations illuminated the binding interactions of WGalNAc with the 5OQV protofibril and provided mechanistic insights into the WGalNAc-mediated structural distortions in the 5OQV protofibril.

Received 26th August 2024,
Accepted 7th March 2025

DOI: 10.1039/d4cp03330b

rsc.li/pccp

1. Introduction

Amyloid fibrils are characteristic of various neurodegenerative diseases like Alzheimer's disease (AD), Parkinson's disease (PD), spongiform encephalopathies, Huntington's disease, and amyotrophic lateral sclerosis (ALS).[1,2] AD is the most widespread type of dementia affecting ∼55 million people worldwide and the most common neurodegenerative

Department of Chemistry & Biochemistry, Thapar Institute of Engineering & Technology, Patiala, 147004, Punjab, India. E-mail: bhupesh@iitbombay.org, bhupesh@thapar.edu

† Electronic supplementary information (ESI) available: The best-docked pose of the 5OQV protofibril and WGalNAc, docked poses of the 5OQV protofibril with WGalNAc with variable distance and position, a 2D interaction map depicting hydrophobic contacts between the 5OQV protofibril and WGalNAc with variable distance and position, comparison of MD ensembles with experimental data, evolution of microstates in the 5OQV protofibril and 5OQV protofibril–WGalNAc during simulation, RMSD and R_g of simulations with different initial velocities, time evolution of the contacts between WGalNAc and residues of the CHC region of the 5OQV protofibril, the number of contacts between the 5OQV protofibril and WGalNAc, and hydrogen bonds of WGalNAc with chains A–D of the 5OQV protofibril during simulation, impact of WGalNAc on the side chain contacts within the hydrophobic core 1 of the 5OQV protofibril in the repeat simulations, WGalNAc-induced modulation in intra- and interchain side chain contacts in the 5OQV protofibril, variations in the angle between planes of Phe19 (chain A) of the 5OQV protofibril and the indole moiety of Trp of WGalNAc during simulation, hydrophobic contacts of WGalNAc with the 5OQV protofibril in the representative conformations, the number of contacts of WGalNAc with the residues of the 5OQV protofibril during simulation, variation of the kink angle in the 5OQV protofibril and 5OQV protofibril–WGalNAc in the repeat simulations, and variations in the polar solvation energies of the 5OQV protofibril, WGalNAc, and 5OQV protofibril–WGalNAc during simulation are shown in Fig. S1–S17. The AutoDock Vina binding energy and key residues of the 5OQV protofibril involved in binding with WGalNAc, top three docked conformations of WGalNAc with the 5OQV protofibril, binding energy and key interactions of the 5OQV protofibril with WGalNAc at varied distance and position, comparative analysis of docked poses from AutoDock Vina and MVD, variation in RMSD of chains A–D of the 5OQV protofibril in simulated systems, details of clustering analysis, binding free energy analysis, and ADMET properties of WGalNAc are presented in Tables S1–S9. See DOI: https://doi.org/10.1039/d4cp03330b

disorder.[3] Based on the data, it is estimated that the health cost of dealing people with AD may rise to US$1.3 trillion by 2050.[3] AD is distinguished by continuous memory loss, mood swings, abnormal behavior, and other cognitive impairments.[4]

The extracellular amyloid-β (Aβ) aggregates and the intracellular neurofibrillary tangles composed of microtubule-associated tau (τ) protein are the pathological hallmarks of AD.[5] The most excessive Aβ isoforms are $A\beta_{42}$ and $A\beta_{40}$, which are derived from the β- and γ-secretase mediated cleavage of the amyloid-β precursor (APP) protein.[6] Literature studies reported that $A\beta_{42}$ displayed a higher neurotoxicity and fibrillation tendency as compared to $A\beta_{40}$.[7] The Aβ aggregates into mature amyloid fibrils through a complex multistep process, which involves the formation of toxic oligomers and protofibrils.[1a,8] The Aβ aggregates are predominantly β-sheet rich structures and adopt various morphologies like U-shaped,[9] S-shaped,[9a,10] or LS-shaped.[11] The main therapeutic interventions to reduce neurotoxic Aβ protofibrils, *i.e.*, blocking the conformational changes of the Aβ monomer and disaggregating Aβ protofibrils, have attracted significant attention.[12] Numerous small molecules,[13] peptides,[14] multitarget-directed ligands,[14b,15] nanoparticles,[16] and antibodies[17] have been explored as prospective inhibitors that block Aβ aggregation and/or disrupt Aβ fibrils. Several studies illuminated the inhibitory mechanisms[18] of various inhibitors against Aβ fibrillation and disruption of protofibrils using molecular dynamics (MD) simulations.

Aromatic amino acids play a crucial role during self-assembly, leading to the formation of amyloid aggregates, as π–π stacking interactions provide energy, order, and directionality to enable amyloid assembly.[19] Thus, hybrid molecules derived by conjugating the aromatic amino acids with small molecules have been explored as potential inhibitors of amyloid aggregation as aromatic rings tend to interfere with the self-assembly of aggregating proteins.[20] Mohammed *et al.* reported the binding of D-Trp–Aib at the aggregation-prone region (Lys16–Glu22) of the $A\beta_{42}$ monomer by π–π stacking interactions between Tyr10 of $A\beta_{42}$ and the indole ring of D-Trp-Aib using MD simulations, which, in turn, blocks the conformational transition to the aggregation-competent β-sheet conformation in the $A\beta_{42}$ monomer.[21] Segal and coworkers highlighted the anti-aggregation activity of a naphthoquinone–tryptophan hybrid against the τ-derived amyloidogenic peptide PHF6 ($_{306}$VQIVYK$_{311}$), $A\beta_{42}$, and the human islet amyloid polypeptide (hIAPP) involved in the etiologies of AD and type 2 diabetes (T2D), respectively, using combined experimental and computational studies.[22] However, the poor solubility of this hybrid molecule under aqueous conditions limits its use as a therapeutic candidate.

Glycan functionalization has been reported to increase the half-life, solubility, and specificity of drugs under *in vivo* conditions.[23] Galactose plays a crucial role in many biological processes, making galactosylation a valuable technique for therapeutic delivery.[24] For instance, galactosylated nanocarriers showed enhanced site-specific delivery of anticancer drugs and siRNA.[24a] Galactose has been utilized in the development of vaccines and treatment as well as diagnosis of several diseases.[25] Both D-galactose and D-glucose are highly suitable for drug delivery to the brain as both hexoses are actively transported through BBB.[26] Galactose-conjugated dopamine demonstrated improved bioavailability, BBB permeability, and therapeutic efficacy in treating PD.[27]

The modification of a β-sheet breaker (BSB) peptide iAβ5p (LPFFD) by conjugating trehalose yielded three glycopeptides with inhibitory activity against $A\beta_{42}$ fibrillation.[28] The trehalose-conjugated peptides (Th-SC, Th-CT, and Th-NT) reduced $A\beta_{42}$ fibrillation to about 40% in NEM (*N*-ethylmaleimide) buffer at a 5-fold molar excess [$A\beta_{42}$ (25 μM) : glycopeptides (125 μM)]. The MTT assay revealed that all the glycopeptides protected cells against Aβ-mediated cytotoxicity upon the second treatment (*i.e.* at the time of $A\beta_{42}$ addition and 48 h later). Segal and coworkers synthesized three different tryptophan–glucosamine conjugates and explored their ability to attenuate the fibrillation of a tau-derived peptide PHF6 peptide.[29] The thioflavin S (ThS) fluorescence, CD, TEM, and *in silico* studies depicted that tryptophan–glucosamine conjugates blocked PHF6 fibrillation as well as disassembled preformed fibrils in a concentration-dependent manner at a molar ratio of 50 : 1 (PHF6 : conjugate). Frenkel-Pinter *et al.* reported selective inhibition of fibrillation and cytotoxicity of a tau-derived peptide 7aa (Ac-SVQIVYK-NH_2) in the presence of its glycosylated analogues [β-linked galactose (Gal), glucosamine (GlcN), and *N*-acetylglucosamine (GlcNAc)] using various biophysical techniques.[30] The ThS fluorescence, CD, and TEM studies highlighted that glycosylation notably decreased the fibrillation of 7aa and resulted in efficiently blocking aggregation of the tau-derived peptide PHF6 peptide by 7aa.

Recently, Paul *et al.* evaluated highly soluble tryptophan–galactosylamine conjugates for their ability to block $A\beta_{42}$ fibrillation and disaggregate fibrils.[31] Among various synthesized hybrid molecules, WGalNAc displayed the best inhibitory potential against $A\beta_{42}$ aggregation and disrupted pre-formed $A\beta_{42}$ assemblies. The ThT kinetic results revealed 61% disaggregation of the pre-formed $A\beta_{42}$ fibrils in the presence of WGalNAc. The CD studies depicted a substantial decline of β-sheet content in the pre-formed $A\beta_{42}$ fibrils upon incubation with WGalNAc. The transmission electron microscopy (TEM) images depicted no fibrillar network in the pre-formed $A\beta_{42}$ assemblies upon the incorporation of WGalNAc.

Furthermore, WGalNAc displayed no toxicity (≥95% viability) upon incubation with SH-SY5Y or HEK-293 cell lines at a concentration of 250 μM. The mammalian cell line-based assays showed that a 20-fold excess of WGalNAc increased the viability of SH-SY5Y cells up to 62.9 ± 2% with an EC_{50} value of 2.3 μM against $A\beta_{42}$ pre-formed fibrils. Moreover, WGalNAc displayed less immunogenicity, enhanced proteolytic stability, and showed blood–brain barrier (BBB) permeability. The *in vitro* and cell-based assays depicted WGalNAc as a potential therapeutic candidate for AD therapy. However, the molecular mechanism through which WGalNAc interacts with $A\beta_{42}$ assemblies leading to its destabilization is not clear. Thus, the disruption mechanism of WGalNAc against $A\beta_{42}$

protofibrils is explored using MD simulations. To our knowledge, this work is the first to delineate the WGalNAc-induced structural distortions in $A\beta_{42}$ protofibrils. The studies illuminating the destabilization mechanism of various inhibitors against the toxic $A\beta_{42}$ oligomers of varying size are worthy for developing new inhibitors of $A\beta_{42}$ fibrillation with the protofibril disruptive effect in AD.

2. Computational details

2.1. Structural details of $A\beta_{42}$ protofibril and WGalNAc

The MD simulations of the $A\beta_{42}$ protofibril alone and in the presence of WGalNAc (designated as the 5OQV protofibril and 5OQV protofibril–WGalNAc, respectively) have been performed in this work (Table 1). The LS-shaped $A\beta_{42}$ protofibril (PDB: 5OQV)[11] was chosen to elucidate the destabilization potential of WGalNAc as it is reported as the smallest stable full-length structure of $A\beta_{42}$ protofibrils [Fig. 1(a and b)],[32] whereas other structures are Aβ fragments (PDB: 2MXU $A\beta_{11-42}$,[33] 5KK3 $A\beta_{11-42}$,[10] 2BEG $A\beta_{17-42}$,[34] 2LMN $A\beta_{9-40}$,[35] and 5AEF $A\beta_{15-42}$[36]). The single chain of the 5OQV protofibril comprises three β-strand regions β1 (3–22), β2 (28–35), and β3 (41–42) along with a kink at Tyr10.[11] Notably, hydrophobic cores (core 1: Ala2, Phe4, Leu34, and, Val36; core 2: Leu17, Phe19, and, Ile31, and core 3: Ala30, Ile32, Met35, and, Val40) and Lys28–Ala42 salt bridge interactions stabilize the LS-shaped morphology of the 5OQV protofibril (Fig. 1a).[11] The 2D chemical structure of WGalNAc was drawn using ChemDraw Ultra 16.0 (Fig. 1c).[37] The WGalNAc structure was energy minimized using Chem3D Ultra and geometry was optimized using Gaussian09[38] and the Hartree–Fock (HF) method with the 6-31G* basis set.[39] The AMBER99SB-ILDN force field[40] parameters for WGalNAc were elucidated using Automated Topology Builder (ATB).[41] Numerous studies have employed ATB to generate initial ligand topologies.[39b,42]

Table 1 MD simulation details for the chosen systems

System	Simulation time (ns)	Box dimensions (nm)	TIP3P water molecules
5OQV protofibril	500 × 3	8.55 × 8.55 × 8.55	**19 677**
5OQV protofibril–WGalNAc	500 × 3	8.55 × 8.55 × 8.55	**19 667**

2.2. Molecular docking

The intermolecular interactions between the 5OQV protofibril and WGalNAc were assessed using AutoDock Vina 1.1[43] and Molegro Virtual Docker (MVD) tools.[44] The PDBQT files for the 5OQV protofibril and WGalNAc were generated using AutoDock tools.[45] The polar hydrogens have been added to the 5OQV protofibril. The Kollman and Gasteiger charges were assigned to the 5OQV protofibril and WGalNAc, respectively, during molecular docking. The 5OQV protofibril was modelled as rigid, while WGalNAc was kept flexible in blind docking. A docking grid of dimensions 114 Å × 126 Å ×116 Å with a grid spacing of 0.436 Å along with axial centers at x = 69.817, y = 48.428, and z = 54.249 was chosen for 5OQV protofibril–WGalNAc. The default exhaustiveness was used and a total of

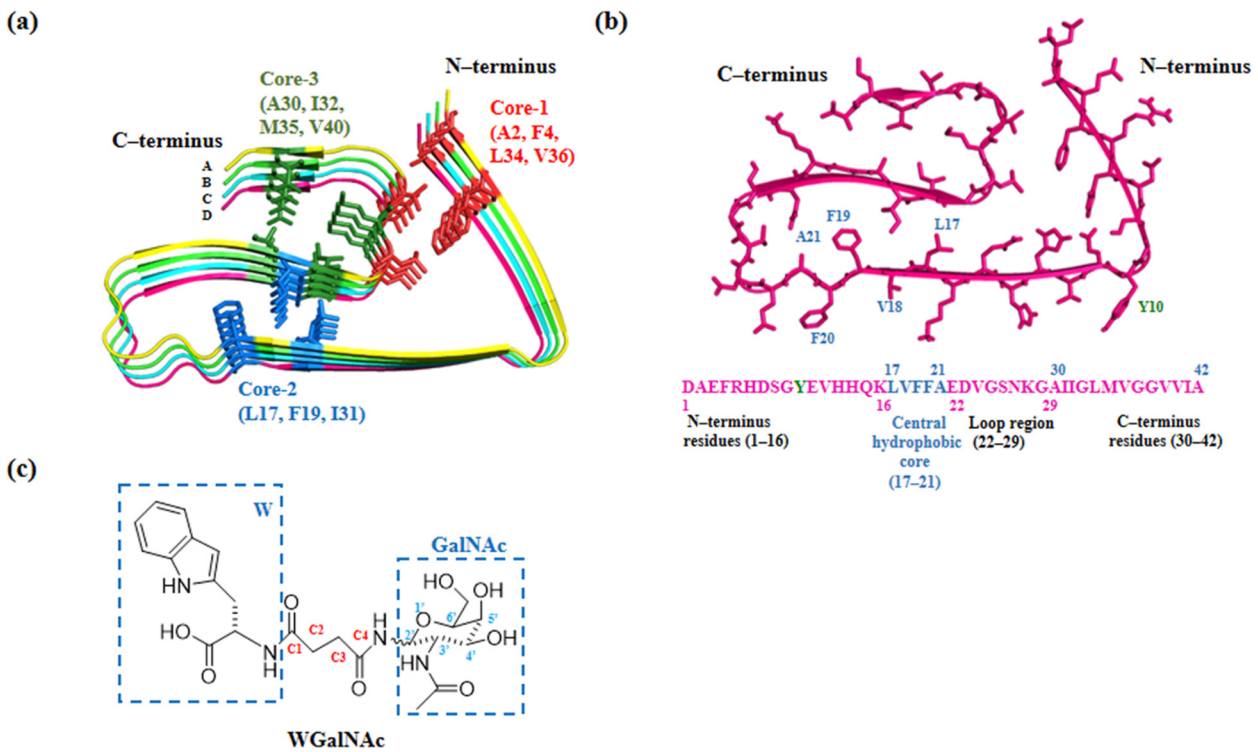

Fig. 1 Cartoon representation of the 5OQV protofibril comprising chains A, B, C, and D with N- and C-termini labeled (panel a). A single chain of protofibrils in the cartoon with side chains in sticks with the $A\beta_{42}$ sequence underneath the cartoon (panel b). The aggregation-competent central hydrophobic core (CHC) region is depicted in blue in the $A\beta_{42}$ sequence. 2D chemical structure of WGalNAc (panel c).

9 docked poses were examined. The Lamarckian genetic algorithm (LGA),[46] which employs Genetic and Solis & Wets[47] algorithms for global and local search, respectively, was employed to produce the docked poses. The docked conformations were examined using AutoDock Tools, PyMOL, and LigPlot+.[45,48]

2.3. MD simulation setup

The conformational ensembles were generated using GROMACS 5.0.7 software.[49] The AMBER99SB-ILDN force field was used as it has been extensively employed to explore the structural changes in the Aβ peptide upon the incorporation of various inhibitors.[50] The 5OQV protofibril was kept in a cubic box[51] of dimensions 8.55 × 8.55 × 8.55 nm^3, and the TIP3P water model[52] was used. To preserve the overall neutrality at physiological pH, the addition of 0.15 M NaCl (with the required Na^+ and Cl^- ions) was achieved in each simulated system.[18e,53] Both systems were equilibrated through NVT and NPT for 500 ps at 310 K. The temperature (310 K) was kept constant by the V-scaling method[54] (coupling time constant = 0.1 ps) and pressure (1 bar) was upheld using a Parrinello–Rahman barostat[55] (coupling time constant = 2 ps). A distance of 1.0 nm was set as a cutoff value for short-range van der Waals interactions, whereas the particle mesh Ewald (PME) method[56] was used for evaluating the long-range electrostatic interactions. The LINCS algorithm[57] was used to constrain the bond lengths and the SETTLE algorithm[58] for restraining water molecules (integration time step = 2 fs). To scrutinize the reliability of MD ensembles, simulations of the 5OQV protofibril and 5OQV protofibril–WGalNAc were performed at different initial velocities.

2.4. MD analysis

The trajectories were analyzed using GROMACS tools and the conformational snapshots were visualized using PyMOL.[48b] The gmx rms, gmx gyrate, and gmx sasa were used for structural stability analysis. The impact of WGalNAc on the secondary structures and hydrogen bonds in the 5OQV protofibril was assessed using gmx do_dssp and gmx hbond, respectively. A hydrogen bond was considered when the distance between the donor and the acceptor was $\leq$0.35 nm and the hydrogen-donor–acceptor angle was $\leq 30^\circ$.[39a,50a] The heavy atom contacts between the 5OQV protofibril and WGalNAc were calculated using gmx mindist with a distance cutoff of $\leq$0.54 nm. The influence of WGalNAc on side chain-side chain interactions in the 5OQV protofibril was assessed using gmx mdmat. The clustering analysis was done by the Daura *et al.*[59] approach and conformational clusters were obtained using the gmx cluster tool at a cutoff of 0.35 nm. The centroid distance between two aromatic rings is considered to be $\leq$0.70 nm to form π–π stacking interactions.[60] The π–π interactions can be classified into three categories: parallel (0–30°), herringbone (30–60°), and T-shaped (60–90°).[32,61] The kink angle (θ) at the Tyr10 was determined using gmx angle.

The binding free energy of 5OQV protofibril–WGalNAc was evaluated for 10 ns at 20 ps using the MM-PBSA (molecular mechanics Poisson–Boltzmann surface area) method by utilizing g_mmpbsa.[62] The entropy calculations were neglected while evaluating the binding free energy following previous studies.[63]

2.5. Estimation of NMR chemical shifts and $^3J_{NH-H\alpha}$ coupling constants

The NMR chemical shifts for Cα and Cβ atoms of the characteristic conformation of the highest populated conformational cluster of the 5OQV protofibril were computed using SHIFTX2.[64] The chemical shifts obtained from the simulation data were compared with the chemical shift of the 5OQV protofibril obtained from BMRB (entry = 27212).[65] The TALOS-N program[66] was used to calculate *J*-coupling ($^3J_{NH-H\alpha}$) constants between NH–Hα protons of the 5OQV protofibril using the Karplus[67] equation and they were compared with the $^3J_{NH-H\alpha}$ experimental values.

$$^3J = A\cos^2\theta + B\cos\theta + C$$

where A = 6.4; B = −1.4; and C = 1.9 (units of A, B, and C in Hz) are Karplus parameters and $\theta = \phi - 60^\circ$ (ϕ is the H_N–N–C_α–H_α dihedral angle).

2.6. ADMET properties

ADMETboost software was utilized to predict the ADMET (absorption, distribution, metabolism, excretion, and toxicity) characteristics of WGalNAc.[68] To evaluate the ADMET properties of WGalNAc, the platform ADMETlab 2.0 was used.[69]

3. Results and discussion

3.1. WGalNAc binds in the CHC region of chain A of the 5OQV protofibril

The low molecular weight $A\beta_{42}$ oligomers comprising tetramers, pentamers, and hexamers displayed much higher toxicity to the neuronal cells and led to synaptic dysfunction.[70] Thus, the destabilization potential of WGalNAc towards $A\beta_{42}$ oligomers was examined using $A\beta_{42}$ protofibrils (PDB: 5OQV). The WGalNAc was docked to the 5OQV protofibril to explore the key interactions of WGalNAc with the 5OQV protofibril. WGalNAc was situated distant from the 5OQV protofibril in the initial conformation (Fig. S1, ESI†). However, upon docking, hydrogen bonds were formed with Val18, Phe20, and Glu22 of chain A of the 5OQV protofibril in the most favourable docked conformation, exhibiting a binding energy of –6.60 kcal mol^{-1} (Fig. S1 and Table S1, ESI†). The three highest-ranked docked poses of WGalNAc with the 5OQV protofibril exhibit binding energies ranging from –6.60 to –5.80 kcal mol^{-1} (Table S2, ESI†). Visual inspection of these top three docked conformations reveals the binding of WGalNAc to the same region of the 5OQV protofibril (Table S2, ESI†). The docking results are consistent with Mallesh *et al.*, who reported a binding energy of −6.20 kcal mol^{-1} between $A\beta_{42}$ protofibrils (PDB: 2BEG) and a benzothiazole-based fluorescent probe RM-28 using AutoDock Vina.[71] Another study reported a binding energy of −6.00 kcal mol^{-1} between

$A\beta_{42}$ protofibrils (PDB: 2NAO) and a gallic acid–glutamine conjugate (GA–Q).[72]

Furthermore, the effect of the initial distance and relative position between the 5OQV protofibril and WGalNAc was explored on the binding sites and interactions of WGalNAc with the 5OQV protofibril (Table S3, ESI†). The distance between the 5OQV protofibril and WGalNAc was increased and molecular docking was performed (Fig. S2b, ESI†). The docking results displayed a favourable binding energy of −6.70 kcal mol^{-1} (Table S3, ESI†). WGalNAc was noted to bind in the CHC region of chain A of the 5OQV protofibril forming hydrogen bonds with Phe20 (A) and Glu22 (A) of the 5OQV protofibril (Fig. S2b and Table S3, ESI†), which was almost similar to the docked pose in which the position of WGalNAc was not perturbed (Table S1, ESI†). Moreover, WGalNAc formed hydrophobic contacts with Phe19 (A), Ala21 (A), Asp23 (A), and Gly29 (A) of the 5OQV protofibril (Fig. S3b). Furthermore, the position of WGalNAc was changed and molecular docking was performed (Fig. S2c). WGalNAc binds to Phe20 (A) of the 5OQV protofibril with a favourable binding energy of −7.10 kcal mol^{-1} (Fig. S2c and Table S3, ESI†). Moreover, WGalNAc formed hydrophobic contacts with Val18 (A), Phe19 (A), Asn27 (A), Gly29 (A), Ile31 (A), Phe19 (B), Lys28 (B), Gly29 (B), and Ala30 (B) of the 5OQV protofibril (Fig. S3c and Table S3, ESI†). Overall, docking results highlighted the binding of WGalNAc with the CHC region of the 5OQV protofibril irrespective of the initial distance and position between WGalNAc and the 5OQV protofibril.

The OH of the carboxylic acid of WGalNAc displayed a hydrogen bond (0.23 nm) with the main chain C═O of Val18 of the 5OQV protofibril. The hydrogen atom of the OH group at the 5′ position of galactose moiety of WGalNAc was involved in a hydrogen bond (0.28 nm) with main chain C═O of Phe20 of the 5OQV protofibril. The oxygen atom at the C1 position of WGalNAc displayed a hydrogen bond (0.22 nm) with the main chain NH of Phe20. Other hydrogen bonds were noted between the OH groups present at 4′ and 5′ positions in the galactose ring of WGalNAc with the main chain NH (0.20, 0.30, and 0.30 nm) and C═O of Glu22 (0.25 nm) of the 5OQV protofibril (Fig. 2a). WGalNAc formed hydrophobic contacts with Phe19, Ala21, and Asn27 of chain A of the 5OQV protofibril (Fig. 2b).

Furthermore, the docked pose from MVD highlighted that WGalNAc displayed hydrophobic contacts with the similar residues of the 5OQV protofibril as observed in the AutoDock Vina (Table S4, ESI†), which, in turn, validated the molecular docking results. The examination of the docked poses highlighted the favourable binding of WGalNAc to the aggregation-competent CHC region of chain A of the 5OQV protofibril.

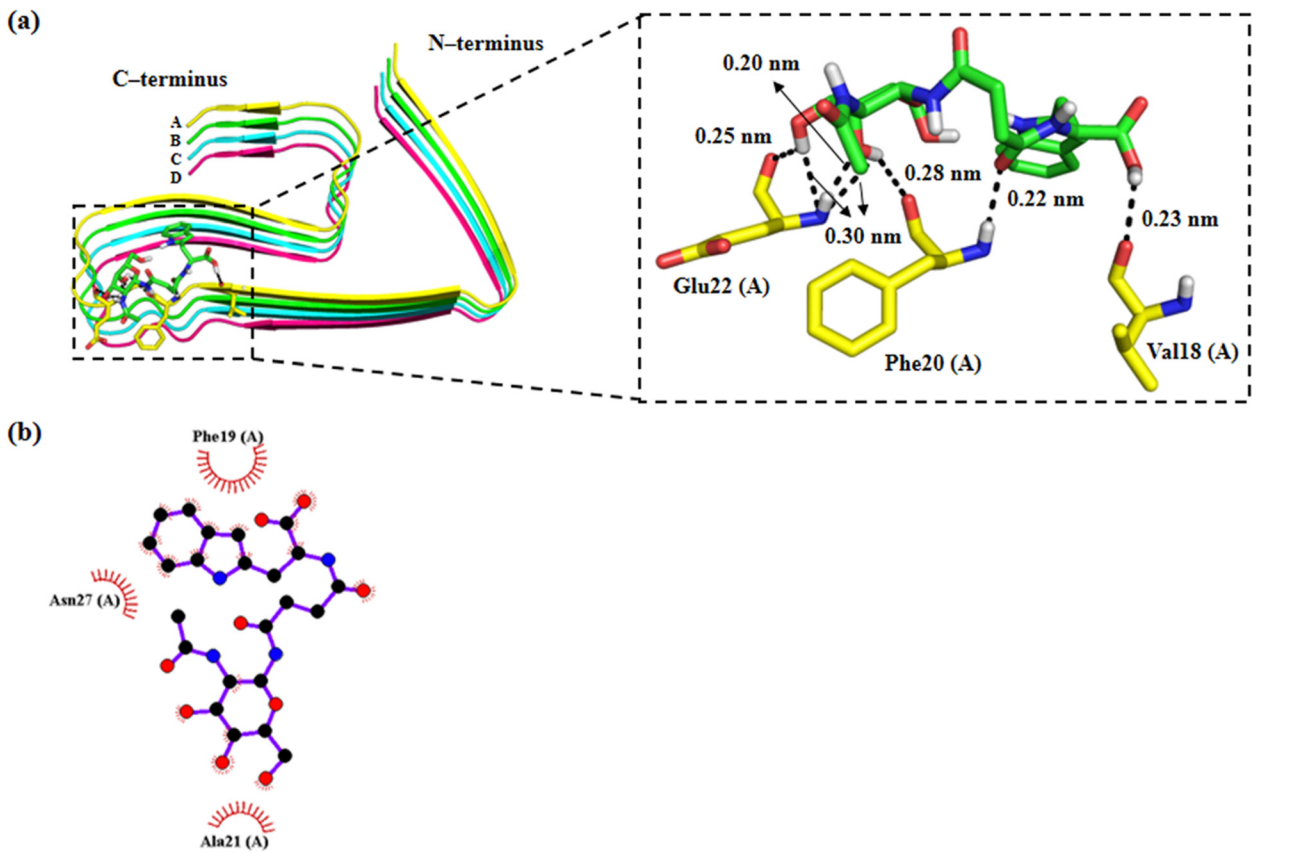

Fig. 2 Illustration of the docked pose of the 5OQV protofibril (cartoon) with WGalNAc (stick) (panel a). WGalNAc displayed hydrogen bonds with chain A residues of the 5OQV protofibril (enlarged view). A 2D interaction map generated using LigPlot+ depicts the hydrophobic contacts between the 5OQV protofibril and WGalNAc (panel b).

Furthermore, atomistic details of the binding of WGalNAc to the $A\beta_{42}$ protofibril leading to its destabilization were examined using MD simulations.

3.2. Comparison of chemical shifts and $^3J_{NH-H\alpha}$ coupling constants between experimental and simulated data of the 5OQV protofibril

A high correlation between the simulated and experimental chemical shift values for the Cα (R^2 = 0.86) and Cβ (R^2 = 0.97) atoms of the 5OQV protofibril has been noted [Fig. S4(a and b), ESI†], which is consistent with the correlation values of Cα and Cβ chemical shifts (0.88 for Cα and 0.96 for Cβ) for the $A\beta_{42}$ protofibril (PDB: 5OQV) reported by Gong *et al.*[73] Additionally, three-bond ^3J-coupling constants were estimated for NH-Hα protons, which better characterize protein structure as compared to primary chemical shifts. A close agreement between the average $^3J_{NH-H\alpha}$ coupling constants obtained from the simulated and experimental data of the 5OQV protofibril was noted (Fig. S4c, ESI†). The high correlation between the simulated and experimental chemical shift values and $^3J_{NH-H\alpha}$ coupling constants highlights the reliability of the 5OQV protofibril conformational ensemble generated by MD simulations.

3.3. Structural stability analysis depicts the disruption of the well-packed β-sheet structure of the 5OQV protofibril upon the incorporation of WGalNAc

For the 5OQV protofibril, an average root mean square deviation (RMSD) of 0.33 ± 0.04 nm was noted during simulation (Fig. 3a). Mohammed *et al.* investigated the destabilization of the $A\beta_{42}$ protofibril (PDB: 2BEG) upon the inclusion of the dipeptide D-Trp-Aib using MD and reported an average backbone RMSD of 0.30 ± 0.01 nm for the protofibril.[21] A noteworthy increase in the RMSD of the 5OQV protofibril from 0.33 ± 0.04 to 0.73 ± 0.17 nm upon the addition of WGalNAc was noted (Fig. 3a), which indicates the opening up of LS-shaped morphology of the 5OQV protofibril.

The conformational sampling was sufficient as the RMSD plots of both systems displayed a converged state for 500 ns simulation, highlighting the steady state of simulated systems (Fig. 3a). Additionally, the conformational ensembles generated by MD were clustered to validate the convergence of the two systems (Fig. S5, ESI†). The convergence of systems was evaluated using the evolution of microstates. For every simulation, it was observed that the MD ensembles reached equilibrium and saturated to specified populations in the microstates defining the converged steady state for both systems.

Furthermore, chain-wise RMSD was calculated to assess the alterations in various chains of the 5OQV protofibril upon the inclusion of WGalNAc (Fig. 3b). Upon the incorporation of WGalNAc, the RMSD of chain A of the 5OQV protofibril was increased from 0.42 ± 0.02 to 0.58 ± 0.03 nm. A significant rise in the RMSD of chain B from 0.34 ± 0.02 nm in the 5OQV protofibril to 0.56 ± 0.03 nm in the 5OQV protofibril-WGalNAc complex was observed. Likewise, a noteworthy increase in the RMSD of chains C and D of the 5OQV protofibril, from 0.31 ± 0.02 to 0.57 ± 0.03 and 0.60 ± 0.03 nm, respectively, was observed upon the inclusion of WGalNAc (Table S5, ESI†). A higher RMSD for each chain of the 5OQV protofibril in the presence of WGalNAc indicates distortions within the LS-shaped protofibrillar structure.

Notably, a higher radius-of-gyration (R_g) of 2.01 ± 0.09 nm was noted for 5OQV protofibril–WGalNAc as compared to 1.75 ± 0.02 nm for the 5OQV protofibril (Fig. 4a), which highlights structural perturbation of the protofibril upon the incorporation of WGalNAc. The R_g of 1.75 ± 0.02 nm in the 5OQV protofibril is consistent with Fang *et al.*, which reported an R_g of 1.72 ± 0.01 nm for the $A\beta_{42}$ pentamer (PDB: 5OQV).[74] Almost similar values of RMSD (0.38 ± 0.02 nm) and R_g (1.75 ± 0.01 nm) for the repeat simulation of the 5OQV protofibril and 5OQV protofibril–WGalNAc (RMSD: 0.69 ± 0.03 nm; R_g: 1.91 ± 0.10 nm) depict the reliability of the MD ensembles (Fig. S6, ESI†). Furthermore, the solvent-accessible surface area (SASA) of the 5OQV protofibril was increased from 109.12 ± 1.19 to 112.51 ± 0.56 nm^2 with the addition of WGalNAc (Fig. 4b), which indicates higher accessibility to the solvent and disruption of the 5OQV protofibril structure. The incorporation of WGalNAc displayed an overall increase of

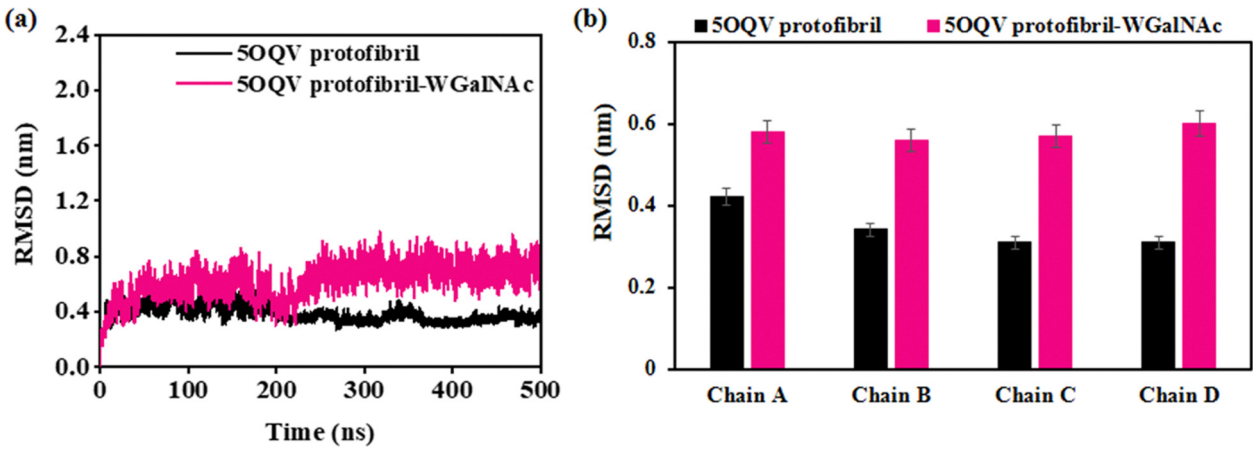

Fig. 3 WGalNAc-induced variations in the overall (panel a) and chain-wise RMSD of the 5OQV protofibril (panel b).

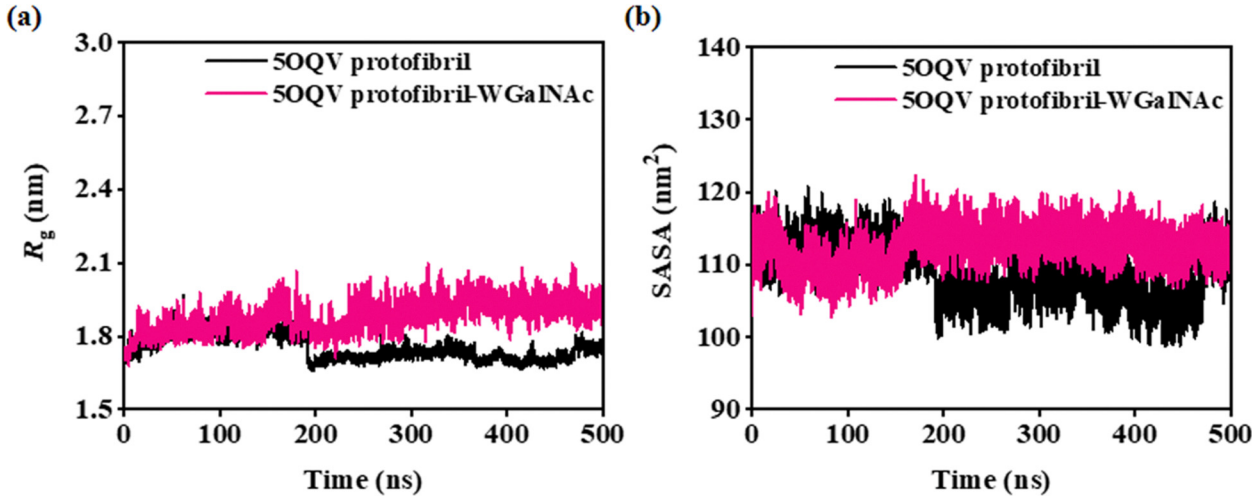

Fig. 4 WGalNAc mediated variations in the R_g (panel a) and SASA (panel b) of the 5OQV protofibril.

$\sim$3.39 nm^2 in SASA for the 5OQV protofibril. A similar increase in the SASA of the Aβ_{42} protofibril upon incorporating licochalcone A ($\sim$2.72 nm^2), licochalcone B ($\sim$4.61 nm^2), EGCG ($\sim$3.99 nm^2), and apigenin ($\sim$4.15 nm^2) has been reported by Fang *et al.*[39a,74]

Additionally, the conformational snapshots of the 5OQV protofibril and 5OQV protofibril–WGalNAc at an interval of 100 ns during simulation depict disorientation of the protofibril chains (Fig. 5). Initially, the protofibrillar chains were close to each other, and LS-shaped morphology was intact in the 5OQV protofibril (Fig. 5, upper panel). However, under the influence of WGalNAc, the protofibril structure became loose and expanded, which indicates the disorganization of the protofibril structure. The disruptive effect of WGalNAc on the 5OQV protofibril structure is evident from the shortening of β-strands at the N- and C-termini, which results in the deformation of the LS-shaped protofibril (Fig. 5, lower panel). The snapshots at 400 and 500 ns depict the detachment of WGalNAc from the CHC region of the 5OQV protofibril (Fig. 5), which is evident from the contact number analysis between WGalNAc and CHC region residues of the 5OQV protofibril (Fig. S7, ESI†). Negligible contacts were observed between WGalNAc and CHC region residues (Leu17, Val18, Phe19, Phe20, and Ala21) of the 5OQV protofibril during 325–500 ns of simulation [Fig. S7(a–e), ESI†], which are consistent with the conformational snapshots at 400 and 500 ns depicting detachment of WGalNAc from the CHC region of the 5OQV protofibril.

3.4. Effect of WGalNAc on the secondary structure content of the 5OQV protofibril

A decrease in the β-sheet content of the 5OQV protofibril from 57.67 ± 0.98 to 54.67 ± 0.54% upon the addition of WGalNAc with a concomitant rise in the coil content from 29.00 ± 0.82 to 32.67 ± 0.72% was observed (Table 2). This aligns with the CD studies, which depicted a substantial reduction in β-sheet content in the pre-formed Aβ_{42} fibrils confirmed by the decreased intensity of a negative peak at $\sim$214 nm in the presence of WGalNAc.[31]

Furthermore, the decrease in the β-sheet content of the 5OQV protofibril concurs well with Gao *et al.*,[50b] who

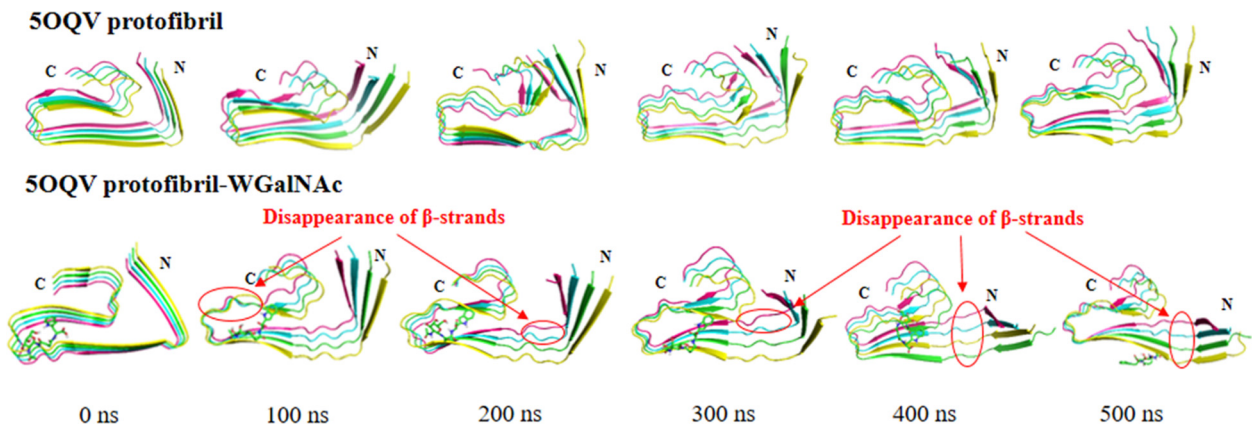

Fig. 5 Snapshots depicting the structural changes in the 5OQV protofibril (upper panel) and 5OQV protofibril–WGalNAc (lower panel) during simulation.

Table 2 WGalNAc-induced conformational changes in the 5OQV protofibril

Secondary structure content (%)	5OQV protofibril	5OQV protofibril–WGalNAc
Helix	0.00 ± 0.00	0.00 ± 0.00
β-sheet[a]	57.67 ± 0.98	54.67 ± 0.54
Coil	29.00 ± 0.82	32.67 ± 0.72
Bend	11.33 ± 0.27	10.66 ± 0.27
Turn	0.00 ± 0.00	0.00 ± 0.00
Chain_separator	2.00 ± 0.00	2.00 ± 0.00

[a] β-sheet = β-strand + β-bridge.

reported a decreased β-sheet content of the $A\beta_{42}$ protofibril (PDB: 5OQV) upon incorporating protonated and deprotonated norepinephrine. Furthermore, an increase of 3.67% in the coil content is consistent with Fang *et al.*, who reported a similar increase (3.44%) in the coil content of the $A\beta_{42}$ pentamer (PDB: 5OQV) upon the addition of licochalcone A to destabilize the protofibril structure.[74]

A noteworthy decrease in the β-sheet content of Asp7–Tyr10 and Glu22–Leu34 regions of the 5OQV protofibril was observed in the presence of WGalNAc (Fig. 6a). Concomitantly, WGalNAc increased the coil content in Asp7–Tyr10, Asp23–Leu34, and Val36 of the 5OQV protofibril (Fig. 6b), which indicates the conversion of the β-sheet into a random coil as visualized in the conformational snapshots (Fig. 5). This is consistent with a previous study[73] in which serotonin lowered β-sheet content at the N-terminal, whereas melatonin diminished β-sheet content at the C-terminal region of the $A\beta_{42}$ protofibril (PDB: 5OQV). Notably, a decrease in the β-sheet with a concomitant rise in the coil content was observed for the residues [Leu34 (core 1), Ile31 (core 2), Ala30, and Ile32 (core 3)] of the hydrophobic cores of the 5OQV protofibril upon the incorporation of WGalNAc (Fig. 6). In addition, Val36 of core 1 of the 5OQV protofibril displayed a rise in the coil from 11.76 to 14.12% with the inclusion of WGalNAc (Fig. 6b). A loss of β-sheet and a concomitant increase in the coil content indicated WGalNAc-mediated structural distortions in the 5OQV protofibril.

3.5. WGalNAc destabilizes the 5OQV protofibril by affecting the hydrogen bonds and hydrophobic contacts critical for its structural stability

To assess the proximity and direct contacts of WGalNAc with the 5OQV protofibril, the number of contacts was computed during simulation (Fig. S8, ESI†). The average number of contacts was 343.03 ± 17.15, indicating strong binding interactions between the 5OQV protofibril and WGalNAc. The intramolecular hydrogen bonds in the 5OQV protofibril were reduced from 118.05 ± 5.90 to 116.80 ± 5.84 with the addition of WGalNAc (Fig. 7a), which depicts the destabilization of the 5OQV structure.

Fang *et al.* reported a marginal decline in intramolecular hydrogen bonds in the $A\beta_{42}$ protofibril (PDB: 2BEG) from 76 ± 4 to 74 ± 7 upon the addition of EGCG.[39a] Furthermore, the hydrogen bonds between WGalNAc and the 5OQV protofibril have been evaluated during simulation and the average intermolecular hydrogen bonds were noted to be 1.50 ± 0.07 (Fig. 7b). This is consistent with Mohammed *et al.*, who depicted the interaction of D-Trp–Aib with the $A\beta_{42}$ protofibril (PDB: 2BEG) involving one or two hydrogen bonds.[21] The hydrogen bond analysis depicted the ability of WGalNAc to partially break the intramolecular hydrogen bonds in the 5OQV

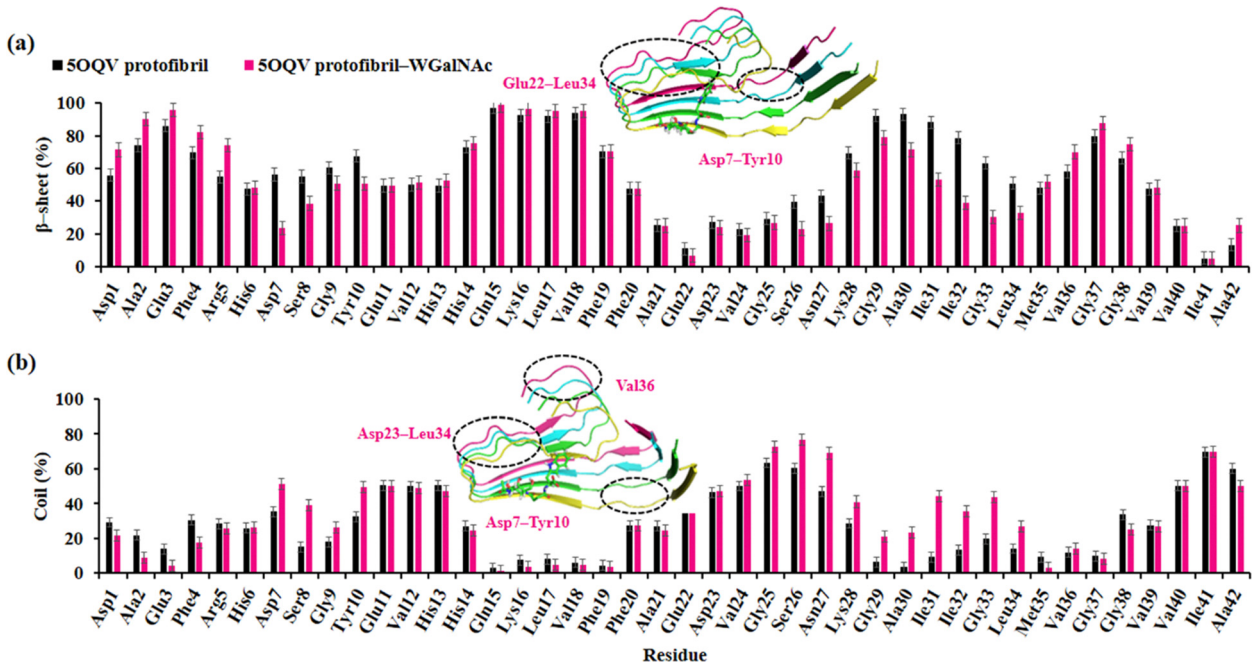

Fig. 6 Residue-wise variation in the β-sheet (panel a) and coil contents (panel b) of the 5OQV protofibril upon the incorporation of WGalNAc. Conformational snapshots depict reduced β-sheet and increased coil contents in 5OQV protofibril residues (shown in black circles).

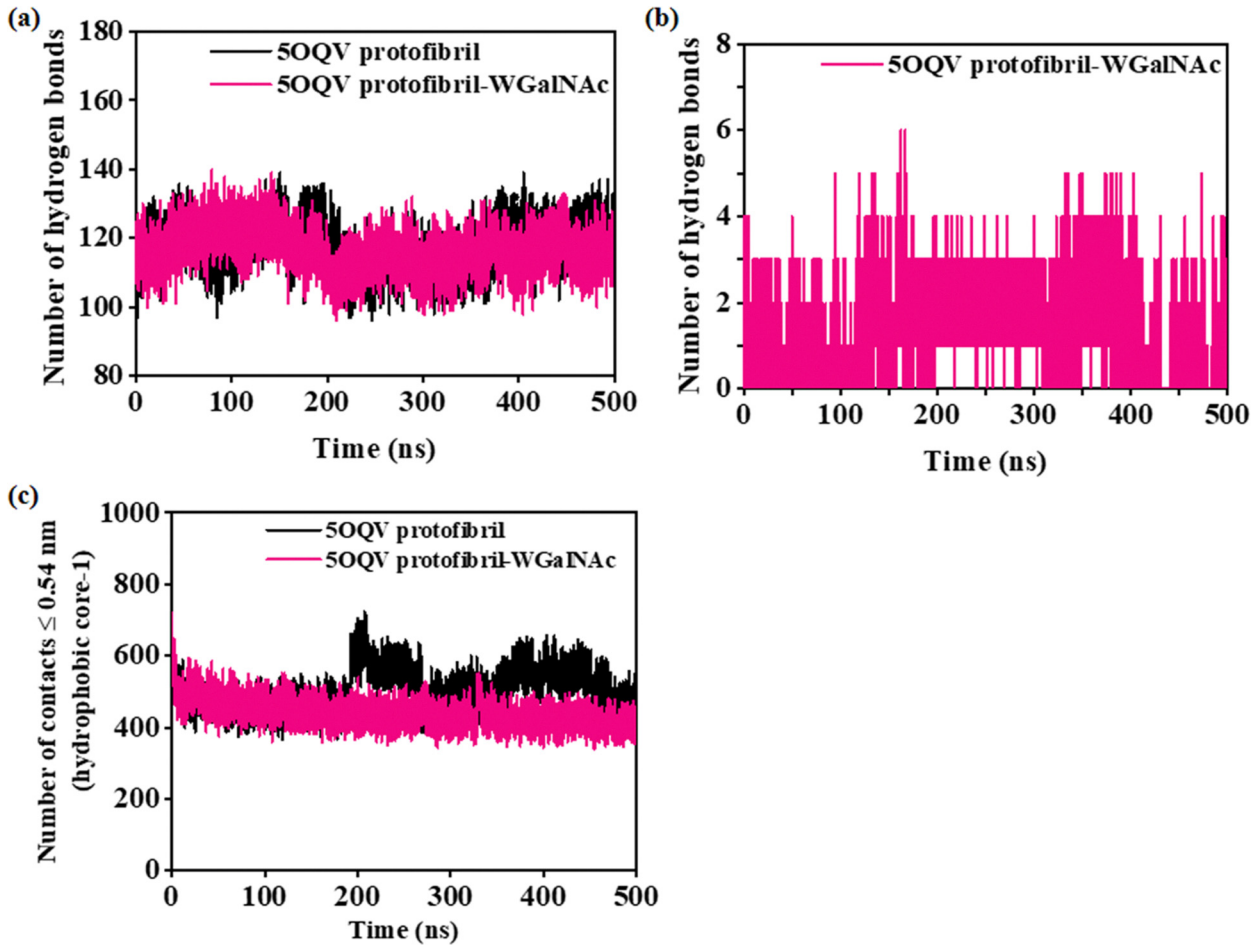

Fig. 7 WGalNAc modulates intramolecular hydrogen bonds in the 5OQV protofibril (panel a). Time-dependent variations in hydrogen bonds between the 5OQV protofibril and WGalNAc (panel b). WGalNAc influences contact within the hydrophobic core-1 of the 5OQV protofibril (panel c).

protofibril and simultaneously form hydrogen bonds with the CHC residues of the 5OQV protofibril.

Moreover, WGalNAc exhibited an average of 1.22 ± 0.06, 0.10 ± 0.01, 0.10 ± 0.01, and 0.06 ± 0.01 hydrogen bonds with the residues of chains A, B, C, and D, respectively, of the 5OQV protofibril (Fig. S9, ESI†). Significantly more hydrogen bonds between WGalNAc and chain A of the 5OQV protofibril indicate a higher binding affinity of WGalNAc with the residues of chain A of the 5OQV protofibril, consistent with the docking analysis (Fig. 2).

The hydrophobic contacts between Ala2, Phe4, Leu34, and Val36 situated in the hydrophobic core 1 of the 5OQV protofibril were mainly responsible for maintaining the stability of the LS-shaped morphology of the protofibril.[11] The side chain contacts within the hydrophobic core were significantly decreased from 503.60 ± 25.18 to 439.88 ± 21.99 upon the incorporation of WGalNAc (Fig. 7c). Furthermore, incorporation of WGalNAc resulted in a decrease of the side chain contacts within the hydrophobic core 1 of the 5OQV protofibril from 541.28 ± 27.06 to 517.17 ± 25.86 and 523.54 ± 26.18 to 496.34 ± 24.82 in the repeat simulations 2 and 3 of 500 ns, respectively (Fig. S10, ESI†). Thus, hydrophobic contacts within the hydrophobic core 1 of the 5OQV protofibril were disrupted by the addition of WGalNAc, which, in turn, led to the disorientation of the LS-shaped 5OQV protofibril. This is consistent with the TEM images that depicted no fibrillar network in the pre-formed $A\beta_{42}$ assemblies upon the incorporation of WGalNAc.[31]

3.6. WGalNAc reduced the side-chain contacts and weakened the stability of the 5OQV protofibril

The toxic protofibrils are formed by misfolding and aggregation of $A\beta_{42}$ fragments,[75] and N- and C-terminus residues of $A\beta_{42}$ play a major role in their aggregation.[76,77] The analysis of intrachain side chain-side chain contacts highlighted that the tertiary contacts formed between N- and C-terminus residues, including hydrophobic core 1 residues of chain A (Ala2–Tyr10 and Gly33–Val40) and chains B–D (Asp1–Tyr10 and Gly33–Val40) of the 5OQV protofibril, completely disappeared in the presence of WGalNAc (Fig. 8 and Fig. S11(a–f), ESI†). Moreover, interchain side chain-side chain contact analysis depicted that residue contacts of Ala2–Tyr10 with Ile32–Val40 involving hydrophobic core 1 residues between different chains (A–B, B–C, and C–D) of the 5OQV protofibril were disrupted upon the

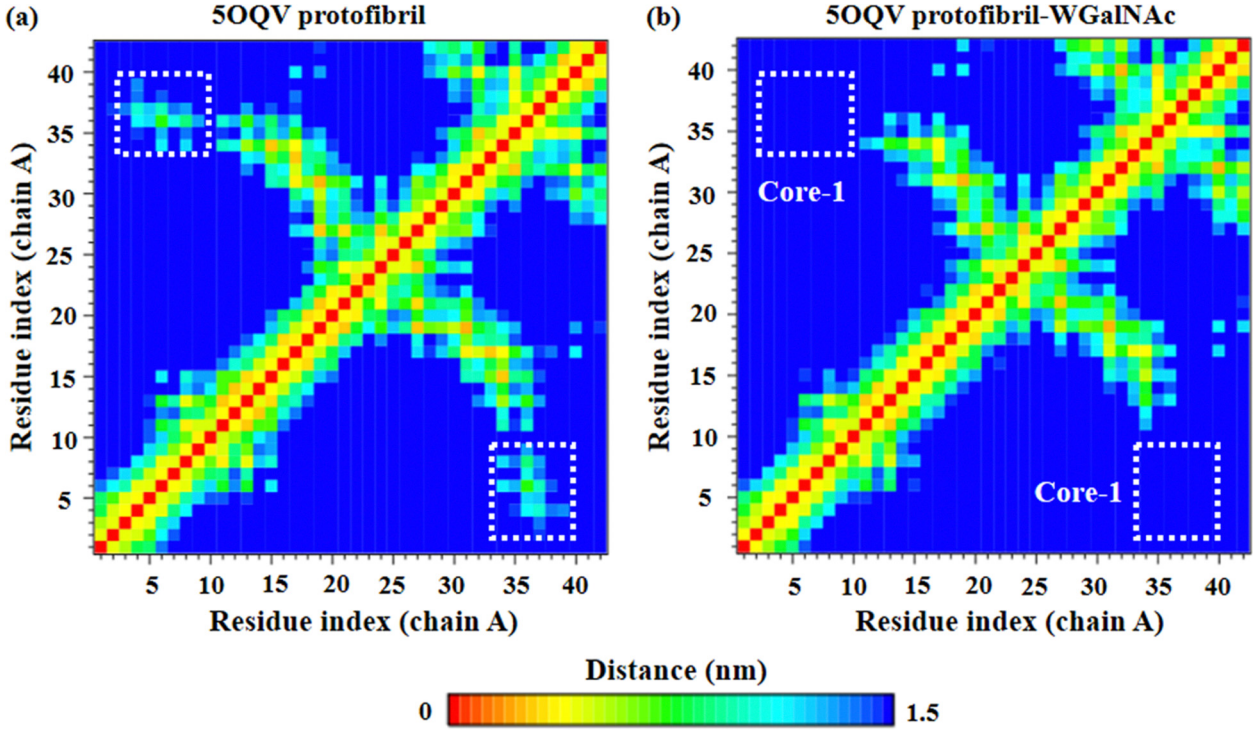

Fig. 8 WGalNAc modulates intrachain side-chain contacts in chain A of the 5OQV protofibril.

incorporation of WGalNAc [Fig. S12(a–f), ESI†]. Overall, the results are consistent with the disruption of side chain contacts in the hydrophobic core 1 of the 5OQV protofibril in the presence of WGalNAc (Fig. 7c). Thus, the disappearance of intra- and interchain side chain-side chain contacts in the 5OQV protofibril indicates WGalNAc-induced distortion in the protofibril structure.

The analysis of conformational microstates unveiled structural alterations resulting in distortions within the 5OQV protofibril upon the addition of WGalNAc (Table S6, ESI†). Significantly, a twenty-fold rise in the conformational microstates, increasing from 7 in the 5OQV protofibril to 145 in 5OQV protofibril–WGalNAc, indicates higher conformational variability and reduced structural stability of the 5OQV protofibril upon incorporating WGalNAc. The top three microstate samples with 78.71, 15.55, and 5.39% conformations were observed in the 5OQV protofibril, which were decreased to 34.04, 28.45, and 9.43% in 5OQV protofibril–WGalNAc, indicating a decrease in the conformational stability of the 5OQV protofibril.

Furthermore, the characteristic conformations of the top three clusters were visualized to analyze key binding interactions between the 5OQV protofibril and WGalNAc (Fig. 9). As π–π interactions among aromatic residues play an important role in the thermodynamic stability of amyloids and direct the kinetics of amyloid formation,[78] π–π interactions were examined in the representative member of the populated cluster (m_1) of 5OQV protofibril–WGalNAc (Fig. 9a). The Aβ CHC residues (Phe19 and Phe20) are involved in the π–π stacking interactions in the fibrillar structure and enhance the structural stability of Aβ aggregates.[79] The Phe19 (chain A) of the 5OQV protofibril displayed π–π interaction (0.63 nm) with the indole moiety of tryptophan of WGalNAc in m_1 conformation (Fig. 9a), which, in turn, interferes in the π–π interactions among phenylalanine residues of neighbouring chains, resulting in the loosening of chains of the 5OQV protofibril. To check the stacking pattern of the π–π stacking interactions between Phe19 (chain A) and the indole moiety of tryptophan of WGalNAc, the angle between planes of two aromatic rings was evaluated during simulation (Fig. S13, ESI†). The average angle between Phe19 (chain A) and the indole moiety of tryptophan of WGalNAc was observed to be 73.88° during simulation, which indicates a T-shaped aromatic stacking pattern.

The residues of chain A of the 5OQV protofibril were involved in hydrogen bond formation in m_1, m_2, and m_3. In m_1, the mainchain hydrogen atom of NH and C═O of Phe20 of the 5OQV protofibril displayed hydrogen bonds (0.22 and 0.26 nm) with C═O of C3 and NH of C4 of WGalNAc, respectively. The mainchain hydrogen atom of NH of Glu22 of the 5OQV protofibril formed a hydrogen bond (0.24 nm) with C═O of the acetyl group of WGalNAc in m_1 (Fig. 9a). In m_2, the mainchain C═O of Ala30 of the 5OQV protofibril formed hydrogen bonds (0.22 and 0.27 nm) with hydrogen atoms of OH at the 6′ position and NH attached to C4 of WGalNAc. Another hydrogen bond of distance 0.22 nm was formed by the mainchain hydrogen atom of Ile32 of the 5OQV protofibril with C═O attached to C3 of WGalNAc (Fig. 9b). In m_3, the Phe20 mainchain C═O and hydrogen atom of NH displayed a hydrogen bond (0.26 and 0.30 nm) with the hydrogen atom of NH of the NAc group and with the oxygen atom of C═O at C1,

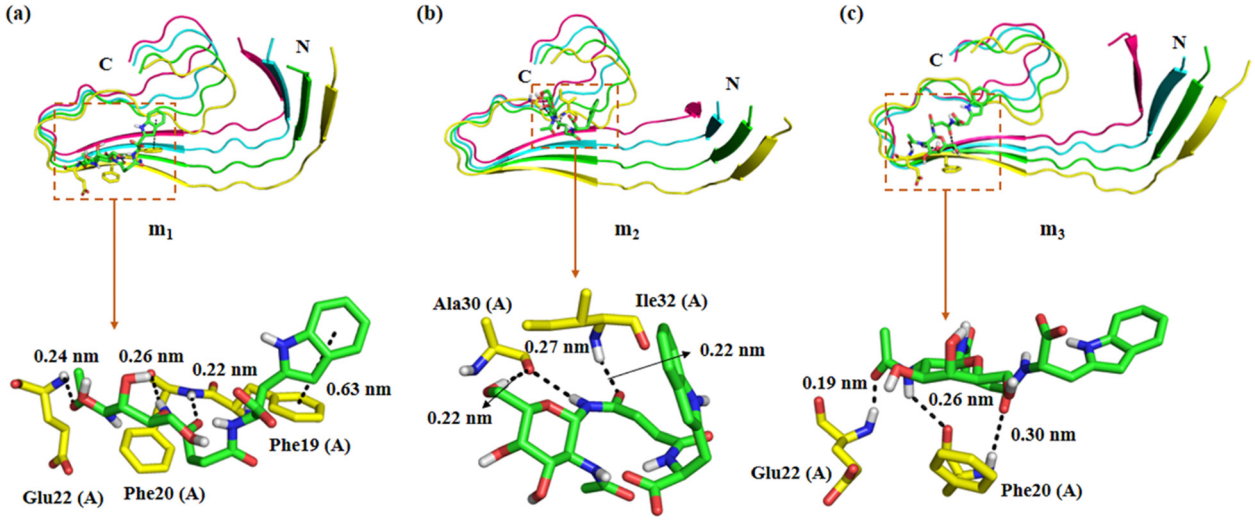

Fig. 9 Representative conformations of the three microstates with the highest conformers in 5OQV protofibril–WGalNAc are shown in the cartoons. The π–π interactions (m_1) and hydrogen bonds (m_1, m_2, and m_3) between the 5OQV protofibril (chain A) and WGalNAc are shown in magnified view underneath the cartoons.

respectively, of WGalNAc. The mainchain hydrogen atom of NH of Glu22 was involved in a hydrogen bond (0.19 nm) with C═O of acetyl of WGalNAc (Fig. 9c).

In m_1, WGalNAc displayed hydrophobic contacts with Phe19 (A), Ala21 (A), Val24 (A), Ala30 (A), Ile31 (A), and Ile32 (A) of the 5OQV protofibril (Fig. S14a, ESI†). Hydrophobic contacts were noticed between Phe19 (A), Ile31 (A), Ile32 (A), and Ala42 (A) of the 5OQV protofibril and WGalNAc in m_2 (Fig. S14b, ESI†). In m_3, WGalNAc formed hydrophobic contacts with Phe19 (A), Phe20 (A), Ala21 (A), Val24 (A), Asn27 (A), Ala30 (A), Ile31 (A), Ile32 (A), and Phe19 (B) of the 5OQV protofibril (Fig. S14c, ESI†). Interestingly, the *N*-acetyl moiety of WGalNAc displayed hydrophobic contacts with Ala21 (A) and Val24 (A) of the 5OQV protofibril in representative conformations [Fig. S14(a and c), ESI†]. The scrutiny of characteristic conformations depicted the importance of tryptophan of WGalNAc in the π–π interactions with Phe19 of 5OQV protofibrils, which is consistent with the experimental study.[31] Furthermore, visualization of representative conformations of the microstates with the highest conformers depicted the involvement of the *N*-acetyl group of WGalNAc in binding with the residues of chain A of the 5OQV protofibril.

Additionally, the average number of contacts between WGalNAc and each residue of the 5OQV protofibril was evaluated (Fig. S15, ESI†). The CHC residues displayed maximum contacts with WGalNAc throughout 500 ns of simulation, highlighting the CHC region as the binding region of WGalNAc at the 5OQV protofibril, which is consistent with conformational clustering analysis (Fig. 9).

3.7. WGalNAc distorts the 5OQV protofibril by alterations in the kink angle

The interactions between His6/His13 and Glu11 stabilize the kink around Tyr10, resulting in the L-shape of the 5OQV protofibril, whereas the Lys28–Ala42 salt bridges stabilize its S-shaped region. The average value for the kink angle was noted to be 84.67° ± 4.23° for the 5OQV protofibril (Fig. 10), which is consistent with the kink angle value of 82° for the 5OQV protofibril determined by Xu *et al.*[50c] Notably, a higher value (89.25° ± 4.46°) of the kink angle was observed upon incorporating WGalNAc, which highlights WGalNAc-induced distortions in the LS-shaped 5OQV protofibril (Fig. 10). Zhan *et al.* reported an increase in the kink angle in the $A\beta_{42}$ protofibril (PDB: 5OQV) to 90° in the presence of stereoisomeric flavonoids (+)-catechin and (−)-catechin.[51c] Furthermore, the average value for the kink angle in the 5OQV protofibril was increased from 85.89° ± 4.29° to 90.88° ± 4.54° and 85.76° ± 4.29° to 89.56° ± 4.48° in the repeat simulations 2 and 3, respectively, in the presence of WGalNAc (Fig. S16, ESI†), which depicts WGalNAc-mediated structural distortions in the LS-shaped 5OQV protofibril.

3.8. Binding free energy and effect of WGalNAc on the interchain interactions in the 5OQV protofibril

The MM-PBSA analysis depicted a favourable binding free energy of −21.76 ± 2.40 kcal mol^{-1} between the 5OQV protofibril and WGalNAc (Fig. 11a and Table S7, ESI†). Singh *et al.* reported a binding free energy of −24.89 ± 0.35 kcal mol^{-1} between the $A\beta_{42}$ protofibril (PDB: 2BEG) and multifunctional cholinergic inhibitor, F24.[80] Hu and coworkers reported a binding free energy of −25.48 ± 6.51 kcal mol^{-1} between the 5OQV protofibril and licochalcone A.[74]

The van der Waals (ΔE_{vdW} = −27.16 ± 1.90 kcal) and nonpolar solvation energies (ΔG_{nps} = −3.12 ± 0.20 kcal mol^{-1}) favoured the binding of WGalNAc to the 5OQV protofibril, whereas the electrostatic term (ΔE_{elec} = 8.17 ± 0.40 kcal mol^{-1}) and polar solvation (ΔG_{ps} = 0.35 ± 1.10) are not favourable (Fig. 11a and Table S7, ESI†). The average value of the polar solvation energies of the 5OQV protofibril, WGalNAc, and 5OQV protofibril–WGalNAc are noted to be −748.50 ± 37.43,

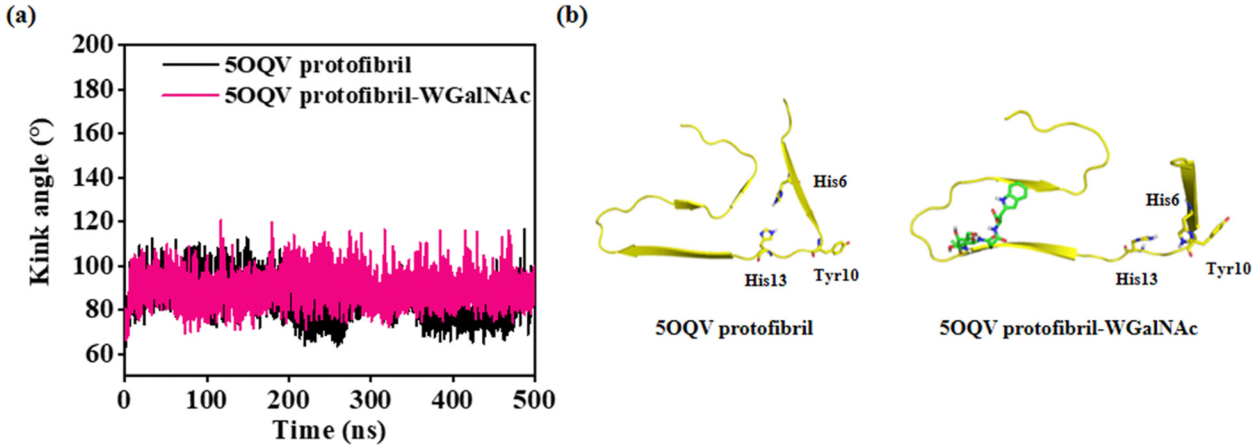

Fig. 10 Variation of the kink angle in the 5OQV protofibril and 5OQV protofibril-WGalNAc during simulation (panel a). The conformational snapshots depict WGalNAc-induced variations in the kink angle, leading to the distortions in the LS-shaped 5OQV protofibril (panel b).

and -22.80 ± 1.14, and -770.95 ± 38.55 kcal mol^{-1}, respectively (Fig. S17, ESI†). From the calculated polar solvation energies, it has been observed that WGalNAc interacts favourably with the solvent. However, the change in polar solvation energy was noted to be unfavourable.

A significant contribution of Phe19 (-2.05 kcal mol^{-1}), Phe20 (-2.99 kcal mol^{-1}), Ile31 (-2.08 kcal mol^{-1}), and Ile32 (-1.56 kcal mol^{-1}) of chain A of the 5OQV protofibril was noted towards binding with WGalNAc (Fig. 12). This is consistent with conformational snapshots depicting the hydrogen bonds between WGalNAc and Phe20 of the 5OQV protofibril in m_1 and m_3 (Fig. 9). Furthermore, π–π interactions between Phe19 (chain A) of the 5OQV protofibril and the benzene ring of tryptophan in WGalNAc noted in the characteristic conformations from the clustering analysis depict strong binding of WGalNAc to the CHC residues Phe19 and Phe20 of chain A of the 5OQV protofibril (Fig. 9). The CHC residues Phe19 and Phe20 in the Aβ monomer play a noteworthy role in the fibrillation of the Aβ monomer to form neurotoxic Aβ oligomers through stacking interactions.[79] The Phe19 and Phe20 of chain A of the 5OQV protofibril were involved in binding with WGalNAc (Fig. 12), which, in turn, prevents the π–π stacking interactions among phenylalanine residues of the B, C, and D chains leading to distortions in the 5OQV protofibril. The high-affinity binding of WGalNAc to the core 2 (Phe19 and Ile31) and core 3 (Ile32) residues of chain A of the 5OQV protofibril interferes with the contacts in the hydrophobic cores of the 5OQV protofibril, resulting in its structural distortion.

To investigate the influence of WGalNAc on the structural distortions in the 5OQV protofibril, the interchain binding free energy was evaluated (Fig. 11b). The binding affinity between the neighbouring chains of the 5OQV protofibril was significantly reduced from -134.31 ± 11.12 to -121.88 ± 1.95 kcal mol^{-1} upon the incorporation of WGalNAc (Table S8, ESI†), which indicates the weakening of the interchain interactions in the 5OQV protofibril. Gong *et al.* reported lowered interchain binding affinity in the $A\beta_{42}$ protofibril (PDB: 5OQV) upon incorporating serotonin and melatonin.[73] Furthermore, the reduced interchain binding affinity in the 5OQV protofibril upon the addition of WGalNAc is consistent with the ThT kinetic assay,[31] which revealed 61% disaggregation of the pre-formed $A\beta_{42}$ fibrils in the presence of WGalNAc. The MD simulation results depicted WGalNAc-mediated structural distortions in the 5OQV protofibril, which are consistent with the experimental results,[31] highlighting

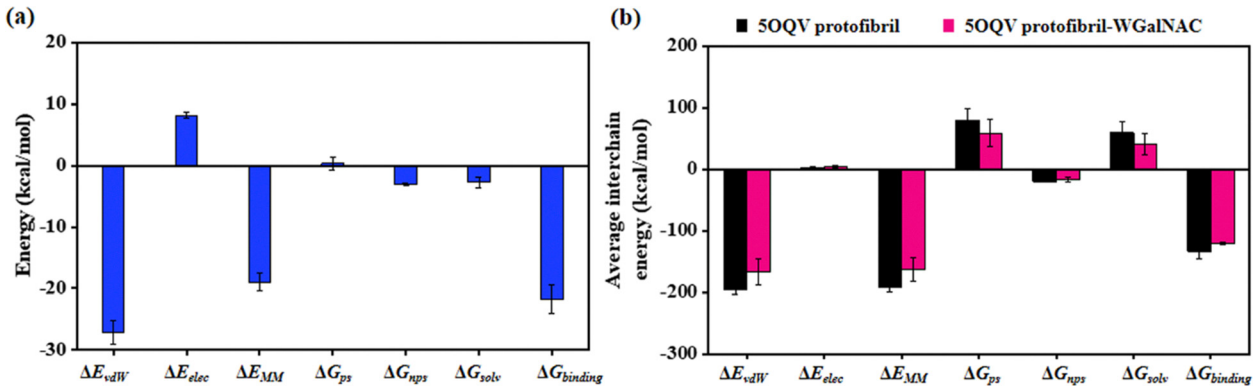

Fig. 11 van der Waals interactions contribute significantly to the binding of WGalNAc to the 5OQV protofibril (panel a). Impact of WGalNAc on the interchain binding affinity in the 5OQV protofibril (panel b).

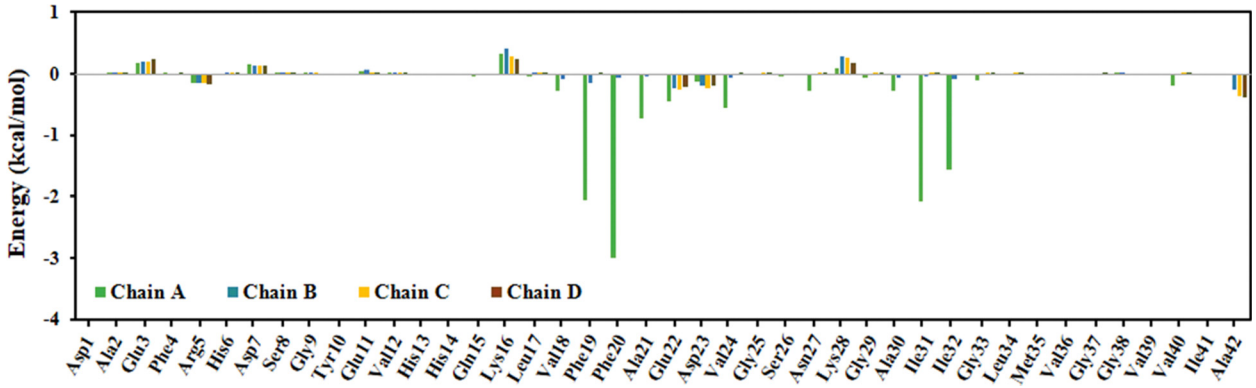

Fig. 12 WGalNAc displayed preferential binding to CHC and C-terminal residues of chain A of the 5OQV protofibril.

disaggregation of the pre-formed $A\beta_{42}$ fibrils upon incubating with WGalNAc, which, in turn, depicts the reliability of the chosen parameters of WGalNAc from the ATB server.[41]

3.9. *In silico* prediction of ADMET properties of WGalNAc

WGalNAc showed optimum lipophilicity ($\log D_{7.4}$), demonstrating its capacity to permeate biological membranes and dissolve in body fluids (Table S9, ESI†). To reach their molecular targets, effective medications targeting the central nervous system (CNS) must cross the BBB. Importantly, WGalNAc demonstrated a potent ability to bind with plasma proteins and penetrate the BBB (Table S9, ESI†). The superior lipophilicity and BBB permeability of WGalNAc make it a good choice to enter the bloodstream and reach its target. Furthermore, WGalNAc did not inhibit the enzymes CYP2C9 or CYP3A4, which are critical for drug metabolism, suggesting that it has no negative impact on other medications. Additionally, WGalNAc is a promising therapeutic candidate for AD due to its extended half-life and non-toxic profile.

The exact nature of the toxic oligomer species responsible for the etiology of AD remains unclear. Thus, studies illuminating the inhibitory mechanism of various inhibitors to destabilize Aβ oligomers of different morphologies (U-shaped,[9] S-shaped,[9a,10] double horse-shoe shaped,[81] and LS-shaped[11]) as well as sizes are worthy for the rational design of new inhibitors to alleviate $A\beta_{42}$ aggregate-induced neurotoxicity in AD. The hydrogen bond interactions and hydrophobic contacts are believed to be critical for the inhibitory potential of the inhibitors; however, all inhibitors do not display identical interactions with the $A\beta_{42}$ monomer/oligomers.[13a,13c,82] Thus, the mechanistic insights into the disruption of the $A\beta_{42}$ protofibril by WGalNAc have been explored using MD simulations in this work, which, in turn, will provide key clues for the rational design of new potent therapeutic candidates against $A\beta_{42}$ fibrillation and disruption of pre-formed neurotoxic oligomers in AD.

4. Conclusions

In this work, the destabilization potential of a highly soluble tryptophan–galactosylamine conjugate WGalNAc against the $A\beta_{42}$ protofibril (PDB: 5OQV) was investigated using computational techniques. WGalNAc binds in the aggregation-prone CHC region of chain A of the 5OQV protofibril. A noteworthy increase in the average RMSD of the 5OQV protofibril upon the addition of WGalNAc indicated a distortion in the LS-shaped 5OQV protofibril. Notably, a decline in the β-sheet content with a concomitant rise in the coil content of the 5OQV protofibril was noted upon the incorporation of WGalNAc, which is consistent with a substantial reduction in β-sheet content in the pre-formed $A\beta_{42}$ fibrils upon incubation with WGalNAc in the CD studies. A noteworthy contribution of Phe19 (-2.05 kcal mol^{-1}) and Phe20 (-2.99 kcal mol^{-1}) of chain A of the 5OQV protofibril to binding with WGalNAc was observed, which, in turn, prevented the π–π interactions between phenylalanine residues of the B, C, and D chains. MM-PBSA analysis depicted reduced binding affinity between the neighbouring chains of the 5OQV protofibril upon adding WGalNAc, which is consistent with the disruption of the side chain contacts between interchain residues, leading to structural distortions in the 5OQV protofibril. MD simulations illuminated the critical role of tryptophan and *N*-acetyl moieties of WGalNAc in the binding interactions with the 5OQV protofibril. The atomistic-level insights into the distortion of the 5OQV protofibril upon the incorporation of WGalNAc illuminated in this work will be highly beneficial for developing highly specific and selective therapeutic candidates to disrupt toxic Aβ oligomers implicated in AD pathogenesis.

Data availability

The computational data related to the findings of this work are available within the article and uploaded supporting information. The software programs available in the public domain have been utilized to generate the data reported in this work. The molecular docking data were obtained using AutoDock Vina 1.1 (**https://vina.scripps.edu/**) and Molegro Virtual Docker (MVD) (**https://molexus.io/molegro-virtual-docker/**) tools. The molecular dynamics simulation data were generated using GROMACS (**https://www.gromacs.org/**). The NMR chemical shifts for Cα and Cβ atoms of the characteristic conformation

of the highest populated conformational cluster of the 5OQV protofibril were computed using SHIFTX2 (https://www.shiftx2.ca/). The binding free energy of 5OQV protofibril–WGalNAc was evaluated using the MM-PBSA (molecular mechanics Poisson–Boltzmann surface area) method by utilizing g_mmpbsa available in GROMACS. The trajectories were analyzed using GROMACS tools and the conformational snapshots were visualized using PyMOL (https://pymol.org/2/). The ADMET properties of WGalNAc were evaluated using the platform ADMETlab 2.0 (https://admetmesh.scbdd.com/). The data were analyzed using Origin (plots and statistics, https://www.originlab.com/). The figures were prepared using Microsoft Powerpoint (https://www.microsoft.com/en-in/microsoft-365/powerpoint) and Adobe Photoshop CS3 Extended (https://www.adobe.com/).

Conflicts of interest

The authors declare no conflict of interest.

Acknowledgements

BG thanks SERB, India (CRG/2023/000088 and CRG/2022/008244) and CSIR, India [02(0451)/21/EMR-II] for the research funding. The authors acknowledge the Department of Chemistry & Biochemistry, TIET Patiala, India for providing research infrastructure.

References

1 (*a*) P. H. Nguyen, A. Ramamoorthy, B. R. Sahoo, J. Zheng, P. Faller, J. E. Straub, L. Dominguez, J.-E. Shea, N. V. Dokholyan, A. De Simone, B. Ma, R. Nussinov, S. Najafi, S. T. Ngo, A. Loquet, M. Chiricotto, P. Ganguly, J. McCarty, M. S. Li, C. Hall, Y. Wang, Y. Miller, S. Melchionna, B. Habenstein, S. Timr, J. Chen, B. Hnath, B. Strodel, R. Kayed, S. Lesné, G. Wei, F. Sterpone, A. J. Doig and P. Derreumaux, Amyloid oligomers: A joint experimental/computational perspective on Alzheimer's disease, Parkinson's disease, Type II diabetes, and Amyotrophic Lateral Sclerosis, *Chem. Rev.*, 2021, **121**, 2545–2647; (*b*) P. H. Nguyen, F. Sterpone and P. Derreumaux, Aggregation of disease-related peptides, *Prog. Mol. Biol. Transl. Sci.*, 2020, **170**, 435–460; (*c*) M. G. Iadanza, M. P. Jackson, E. W. Hewitt, N. A. Ranson and S. E. Radford, A new era for understanding amyloid structures and disease, *Nat. Rev. Mol. Cell Biol.*, 2018, **19**, 755–773.

2 (*a*) S. H. W. Scheres, B. Ryskeldi–Falcon and M. Goedert, Molecular pathology of neurodegenerative diseases by cryo-EM of amyloids, *Nature*, 2023, **621**, 701–710; (*b*) S. Linse and T. Knowles, Amyloids and protein aggregation, *Chem. Sci.*, 2023, **14**, 6491–6492; (*c*) A. K. Buell, Stability matters, too–the thermodynamics of amyloid fibril formation, *Chem. Sci.*, 2022, **13**, 10177–10192; (*d*) C. Soto and S. Pritzkow, Protein misfolding, aggregation, and conformational strains in neurodegenerative diseases, *Nat. Neurosci.*, 2018, **21**, 1332–1340; (*e*) F. Chiti and M. C. Dobson, Protein misfolding, amyloid formation, and human disease: A summary of progress over the last decade, *Annu. Rev. Biochem.*, 2017, **86**, 27–68.

3 https://www.alzint.org/resource/attitudes-to-dementia-world-alzheimer-report-2024-survey-information/ (Date of access: August 25, 2024).

4 (*a*) H. Hippius and G. Neundörfer, The discovery of Alzheimer's disease, *Dialogues Clin. Neurosci.*, 2003, **5**, 101–108; (*b*) A. Alzheimer, Über Eine Eigenartige Erkrankung Der Hirnrinde, *Allg. Zschr. Psychiat. Psychol. Gerichtl. Med.*, 1907, **64**, 146–148.

5 (*a*) K. Ono, Alzheimer's disease as oligomeropathy, *Neurochem. Int.*, 2018, **119**, 57–70; (*b*) A. J. Sierra-Fonseca and L. K. Gosselink, Tauopathy and neurodegeneration: A role for stress, *Neurobiol. Stress*, 2018, **9**, 105–112; (*c*) M. R. Nisbet, C. J. Polanco, M. L. Ittner and J. Götz, Tau aggregation and its interplay with amyloid–β, *Acta Neuropathol.*, 2015, **129**, 207–220; (*d*) S. Bloom, Amyloid-β and tau: The trigger and bullet in Alzheimer disease pathogenesis, *JAMA Neurol.*, 2014, **71**, 505–508; (*e*) D. Eisenberg and M. Jucker, The amyloid state of proteins in human diseases, *Cell*, 2012, **14**, 1188–1203; (*f*) P. M. Murphy and H. LeVine, Alzheimer's disease and the amyloid–β peptide, *J. Alzheimer's Dis.*, 2010, **19**, 311–323; (*g*) M. Goedert and M. G. Spillantini, A century of Alzheimer's disease, *Science*, 2006, **314**, 777–781.

6 (*a*) C. Haass and D. J. Selkoe, Soluble protein oligomers in neurodegeneration: lessons from the Alzheimer's amyloid β-peptide, *Nat. Rev. Mol. Cell Biol.*, 2007, **8**, 101–112; (*b*) J. Hardy and D. J. Selkoe, The amyloid hypothesis of Alzheimer's disease: progress and problems on the road to therapeutics, *Science*, 2002, **297**, 353–356.

7 (*a*) N. J. Economou, M. J. Giammona, T. D. Do, X. Zheng, D. B. Teplow, S. K. Buratto and M. T. Bowers, Amyloid β-protein assembly and Alzheimer's disease: Dodecamers of Aβ42, but not of Aβ40, seed fibril formation, *J. Am. Chem. Soc.*, 2016, **138**, 1772–1775; (*b*) M. A. Findeis, The role of amyloid β peptide 42 in Alzheimer's disease, *Pharmacol. Ther.*, 2007, **116**, 266–286; (*c*) Y. Yan and C. Wang, Aβ42 is more rigid than Aβ40 at the C terminus: Implications for Aβ aggregation and toxicity, *J. Mol. Biol.*, 2006, **364**, 853–862.

8 (*a*) R. Limbocker, N. Cremades, R. Cascella, P. M. Tessier, M. Vendruscolo and F. Chiti, Characterization of pairs of toxic and nontoxic misfolded protein oligomers elucidates the structural determinants of oligomer toxicity in protein misfolding diseases, *Acc. Chem. Res.*, 2023, **56**, 1395–1405; (*b*) A. J. Dear, G. Meisl, A. Šarić, T. C. T. Michaels, M. Kjaergaard, S. Linse and T. P. J. Knowles, Identification of on- and off-pathway oligomers in amyloid fibril formation, *Chem. Sci.*, 2020, **11**, 6236–6247; (*c*) S. J. Bunce, Y. Wang, K. L. Stewart, A. E. Ashcroft, S. E. Radford, C. K. Hall and A. J. Wilson, Molecular insights into the surface-catalyzed secondary nucleation of amyloid-β40 (Aβ40) by the peptide fragment Aβ16–22, *Sci. Adv.*, 2019, **5**, eaav8216; (*d*) S. J. C. Lee, E. Nam, H. J. Lee, M. G. Savelieff and M. H. Lim, Towards an understanding of amyloid-β

oligomers: Characterization, toxicity mechanisms, and inhibitors, *Chem. Soc. Rev.*, 2017, **46**, 310–323; (*e*) C. L. Masters and D. J. Selkoe, Biochemistry of amyloid β-protein and amyloid deposits in Alzheimer disease, *Cold Spring Harbor Perspect. Med.*, 2012, **2**, a006262; (*f*) M. Ahmed, J. Davis, D. Aucoin, T. Sato, S. Ahuja, S. Aimoto, J. I. Elliott, W. E. Van Nostrand and S. O. Smith, Structural conversion of neurotoxic amyloid-β1–42 oligomers to fibrils, *Nat. Struct. Mol. Biol.*, 2010, **17**, 561–567; (*g*) S. L. Bernstein, N. F. Dupuis, N. D. Lazo, T. Wyttenbach, M. M. Condron, G. Bitan, D. B. Teplow, J. E. Shea, B. T. Ruotolo, C. V. Robinson and M. T. Bowers, Amyloid-β protein oligomerization and the importance of tetramers and dodecamers in the aetiology of Alzheimer's disease, *Nat. Chem.*, 2009, **1**, 326–331; (*h*) D. M. Walsh and D. J. Selkoe, Aβ oligomers–a decade of discovery, *J. Neurochem.*, 2007, **101**, 1172–1184.

9 (*a*) G. Grasso, M. Rebella, S. Muscat, U. Morbiducci, J. Tuszynski, A. Danani and M. A. Deriu, Conformational dynamics and stability of U-shaped and S-shaped amyloid–β assemblies, *Int. J. Mol. Sci.*, 2018, **19**, 571; (*b*) M. Cheon, K. C. Hall and I. Chang, Structural conversion of Aβ17–42 peptides from disordered oligomers to U-shape protofilaments via multiple kinetic pathways, *PLoS Comput. Biol.*, 2015, **11**, e1004258.

10 M. T. Colvin, R. Silvers, Q. Z. Ni, T. V. Can, I. Sergeyev, M. Rosay, K. J. Donovan, B. Michael, J. Wall, S. Linse and R. G. Griffin, Atomic resolution structure of monomorphic $A\beta_{42}$ amyloid fibrils, *J. Am. Chem. Soc.*, 2016, **138**, 9663–9674.

11 L. Gremer, D. Schölzel, C. Schenk, E. Reinartz, J. Labahn, R. B. G. Ravelli, M. Tusche, C. Lopez-lglesias, W. Hoyer, H. Heise, D. Willbold and G. F. Schroder, Fibril structure of amyloid–β (1–42) by cryo-electron microscopy, *Science*, 2017, **358**, 116–119.

12 (*a*) S. M. Ruttenberg and J. S. Nowick, A turn for the worse: Aβ β-hairpins in Alzheimer's disease, *Bioorg. Med. Chem.*, 2024, **105**, 17715; (*b*) S. C. Bai, Y. C. Wang, X. Z. Li and G. Li, Inhibiting the aggregation of Aβ by natural product molecules, *ChemMedChem*, 2024, **19**, e202400223; (*c*) Z. Zhou, Y. Q. Gu and H. X. Wang, Artificial chiral interfaces against amyloid-β peptide aggregation: Research progress and challenges, *ACS Chem. Neurosci.*, 2021, **12**, 4236–4248; (*d*) V. Armiento, A. Spanopoulou and A. Kapurniotu, Peptide-based molecular strategies to interfere with protein misfolding, aggregation, and cell degeneration, *Angew. Chem., Int. Ed.*, 2020, **59**, 3372–3384; (*e*) S. Gupta and A. K. Dasmahapatra, Caffeine destabilizes preformed Aβ protofilaments: Insights from all atom molecular dynamics simulations, *Phys. Chem. Chem. Phys.*, 2019, **21**, 22067–22080; (*f*) W. J. Du, J. J. Guo, M. T. Gao, S. Q. Hu, X. Y. Dong, Y. F. Han, F. F. Liu, S. Jiang and Y. Sun, Brazilin inhibits amyloid β-protein fibrillogenesis, remodels amyloid fibrils and reduces amyloid cytotoxicity, *Sci. Rep.*, 2015, **5**, 7992.

13 (*a*) Y. Jin, M. A. Downey, A. Singh, S. K. Buratto and M. T. Bowers, Computationally designed small molecules disassemble both soluble oligomers and protofibrils of amyloid β-protein responsible for Alzheimer's disease, *ACS Chem. Neurosci.*, 2023, **14**, 2717–2726; (*b*) S. Oasa, V. L. Kouznetsova, A. Tiiman, V. Vukojevic, I. F. Tsigelny and L. Terenius, Small molecule decoys of aggregation for elimination of Aβ-peptide toxicity, *ACS Chem. Neurosci.*, 2023, **14**, 1575–1584; (*c*) R. Roy and S. Paul, Illustrating the effect of small molecules derived from natural resources on amyloid peptides, *J. Phys. Chem. B*, 2023, **127**, 600–615; (*d*) Y. Sánchez, C. Castillo, J. Fuentealba, F. Sáez-Orellana, C. F. Burgos, J. J. López, A. F. de la Torre and C. A. Jiménez, New benzodihydrofuran derivatives alter the amyloid β peptide aggregation: Strategies to develop new anti-Alzheimer drugs, *ACS Chem. Neurosci.*, 2023, **14**, 2590–2602; (*e*) H. Nedaei, N. Rezaei-Ghaleh, K. Giller, S. Becker, L. Karami, A. A. Moosavi-Movahedi, C. Griesinger and A. A. Saboury, The calcium-free form of atorvastatin inhibits amyloid-β (1–42) aggregation *in vitro*, *J. Biol. Chem.*, 2022, **298**, 101662; (*f*) S. Brogi, H. Sirous, V. Calderone and G. Chemi, Amyloid β fibril disruption by oleuropein aglycone: Long-time molecular dynamics simulation to gain insight into the mechanism of action of this polyphenol from extra virgin olive oil, *Food Funct.*, 2020, **11**, 8122–8132; (*g*) T. D. Martin, A. J. Malagodi, E. Y. Chi and D. G. Evans, A computational study of the driving forces and dynamics of curcumin binding to amyloid–β protofibrils, *J. Phys. Chem. B*, 2019, **123**, 551–560.

14 (*a*) F. Moraca, I. Vespoli, D. Mastroianni, V. Piscopo, R. Gaglione, A. Arciello, M. De Nisco, S. Pacifico, B. Catalanotti and S. Pedatella, Synthesis, biological evaluation and metadynamics simulations of novel N-methyl β-sheet breaker peptides as inhibitors of Alzheimer's β-amyloid fibrillogenesis, *RSC Med. Chem.*, 2024, **15**, 2286–2299; (*b*) K. Singh, A. Kaur, B. Goyal and D. Goyal, Harnessing the therapeutic potential of peptides for synergistic treatment of Alzheimer's disease by targeting Aβ aggregation, metal-mediated Aβ aggregation, cholinesterase, tau degradation, and oxidative stress, *ACS Chem. Neurosci.*, 2024, **15**, 2545–2564; (*c*) N. Sehra, R. Parmar, I. K. Maurya, V. Kumar, K. Tikoo and R. Jain, Synthesis and mechanistic study of ultrashort peptides that inhibits Alzheimer's Aβ-aggregation-induced neurotoxicity, *Bioorg. Chem.*, 2024, **144**, 107159; (*d*) A. Kaur, O. K. Mankoo, D. Rani, N. Priyadarshi, D. Goyal, N. K. Singhal and B. Goyal, Exploring the impact of C-terminal based pentapeptides on the disassembly of $A\beta_{42}$ fibrils, *ChemMedChem*, 2024, **19**, e202400486; (*e*) D. R. Puneeth Kumar, S. A. Nalawade, S. Pahan, M. Singh, D. K. Senapati, S. Roy, S. Dey, S. U. Toraskar, S. Raghothama and H. N. Gopi, Proteolytically stable ααγ-hybrid peptides inhibit the aggregation and cytotoxicity of $A\beta_{42}$, *ACS Chem. Neurosci.*, 2023, **14**, 3398–3408; (*f*) S. Lacham-Hartman, R. Moshe, S. Ben-Zichri, Y. Shmidov, R. Bitton, R. Jelinek and N. Papo, APPI-derived cyclic peptide enhances Aβ42 aggregation and reduces Aβ42-mediated membrane destabilization and cytotoxicity, *ACS Chem. Neurosci.*, 2023, **14**, 3385–3397; (*g*) Y. Tang, D. Zhang and J. Zheng, Repurposing

antimicrobial protegrin-1 as a dual-function amyloid inhibitor via cross-seeding, *ACS Chem. Neurosci.*, 2023, **14**, 3143–3155; (*h*) K. A. Murray, C. J. Hu, S. L. Griner, H. Pan, J. T. Bowler, R. Abskharon, G. M. Rosenberg, X. Cheng, P. M. Seidler and D. S. Eisenberg, De novo designed protein inhibitors of amyloid aggregation and seeding, *Proc. Natl. Acad. Sci. U. S. A.*, 2022, **119**, e2206240119; (*i*) L. Lei, Z. Zou, J. Liu, Z. Xu, Y. Fu, Y. Tian and W. Zhang, Multifunctional peptide-assembled micelles for simultaneously reducing amyloid-β and reactive oxygen species, *Chem. Sci.*, 2021, **12**, 6449–6457; (*j*) S. Bhattacharjee and R. Bhattacharyya, PRFF peptide mimic interferes with toxic fibrin–$A\beta_{42}$ interaction by emulating the Aβ binding interface on fibrinogen, *ACS Chem. Neurosci.*, 2021, **12**, 4144–4152; (*k*) A. Mitra and N. Sarkar, Sequence and structure-based peptides as potent amyloid inhibitors: A review, *Arch. Biochem. Biophys.*, 2020, **695**, 108614; (*l*) J. Kaffy, C. Berardet, L. Mathieu, B. Legrand, M. Taverna, F. Halgand, G. Van Der Rest, L. T. Maillard and S. Ongeri, Helical γ-peptide foldamers as dual inhibitors of amyloid-β Peptide and islet amyloid polypeptide oligomerization and fibrillization, *Chem. – Eur. J.*, 2020, **26**, 14612–14622; (*m*) P. Mondal, J. Khan, V. Gupta and S. Ghosh, *In silico* approach for designing potent neuroprotective hexapeptide, *ACS Chem. Neurosci.*, 2019, **10**, 3018–3030.

15 (*a*) S. Fares, W. M. El Husseiny, K. B. Selim and M. A. M. Massoud, Modified tacrine derivatives as multitarget-directed ligands for the treatment of Alzheimer's disease: Synthesis, biological evaluation, and molecular modeling study, *ACS Omega*, 2023, **8**, 26012–26034; (*b*) K. Luo, J. Chen, H. Li, D. Wu, Y. Du, S. Zhao, T. Liu, L. Li, Z. Dai, Y. Li and Y. Zhao, Design, synthesis and biological evaluation of new multi-target scutellarein hybrids for treatment of Alzheimer's disease, *Bioorg. Chem.*, 2023, **138**, 106596; (*c*) B. Kumar, A. R. Dwivedi, T. Arora, K. Raj, V. Prashar, V. Kumar, S. Singh, J. Prakash and V. Kumar, Design, synthesis, and pharmacological evaluation of N-propargylated diphenylpyrimidines as multitarget directed ligands for the treatment of Alzheimer's disease, *ACS Chem. Neurosci.*, 2022, **13**, 2122–2139; (*d*) M. Rana, H. J. Cho, H. Arya, T. K. Bhatt, K. Bhar, S. Bhatt, L. M. Mirica and A. K. Sharma, Azo-stilbene and pyridine–amine hybrid multifunctional molecules to target metal-mediated neurotoxicity and amyloid-β aggregation in Alzheimer's disease, *Inorg. Chem.*, 2022, **61**, 10294–10309; (*e*) Z. Yang, Q. Song, Z. Cao, G. Yu, Z. Liu, Z. Tan and Y. Deng, Design, synthesis and evaluation of flurbiprofen-clioquinol hybrids as multitarget-directed ligands against Alzheimer's disease, *Bioorg. Med. Chem.*, 2020, **28**, 115374; (*f*) A. Kaur, S. Mann, A. Kaur, N. Priyadarshi, B. Goyal, N. K. Singhal and D. Goyal, Multi-target-directed triazole derivatives as promising agents for the treatment of Alzheimer's disease, *Bioorg. Chem.*, 2019, **87**, 572–584; (*g*) A. Kaur, S. S. Narang, A. Kaur, S. Mann, N. Priyadarshi, B. Goyal, N. K. Singhal and D. Goyal, Multifunctional mono-triazole derivatives inhibit $A\beta_{42}$ aggregation and Cu^{2+}-mediated $A\beta_{42}$ aggregation and protect against $A\beta_{42}$-induced cytotoxicity, *Chem. Res. Toxicol.*, 2019, **32**, 1824–1839; (*h*) D. Goyal, A. Kaur and B. Goyal, Benzofuran and indole: promising scaffolds for drug development in Alzheimer's disease, *ChemMedChem*, 2018, **3**, 1275–1299; (*i*) N. Q. Thai, Z. Bednarikova, M. Gancar, H. Q. Linh, C.-K. Hu, M. S. Li and Z. Gazova, Compound CID 9998128 is a potential multitarget drug for Alzheimer's disease, *ACS Chem. Neurosci.*, 2018, **9**, 2588–2598.

16 (*a*) Y. J. Chang, Y. H. Chien, C. C. Chang, P. N. Wang, Y. R. Chen and Y. C. Chang, Detection of femtomolar amyloid-β peptides for early-stage identification of Alzheimer's amyloid-β aggregation with functionalized gold nanoparticles, *ACS Appl. Mater. Interfaces*, 2024, **16**, 3819–3828; (*b*) N. Andrikopoulos, Y. Li, A. Nandakumar, J. F. Quinn, T. P. Davis, F. Ding, N. Saikia and P. C. Ke, Zinc–epigallocatechin-3-gallate network-coated nanocomposites against the pathogenesis of amyloid-beta, *ACS Appl. Mater. Interfaces*, 2023, **15**, 7777–7792; (*c*) M. Zangiabadi, A. Ghosh and Y. Zhao, Nanoparticle scanners for the identification of key sequences involved in the assembly and disassembly of β-amyloid peptides, *ACS Nano*, 2023, **17**, 4764–4774; (*d*) S. Mandal, D. Jana, J. Dolai, A. K. Sarkar, B. K. Ghorai and N. R. Jana, Biodegradable poly(trehalose) nanoparticle for preventing amyloid beta aggregation and related neurotoxicity, *ACS Appl. Bio Mater.*, 2023, **6**, 2102–2110; (*e*) Y. Wang, W. Liu, X. Dong and Y. Sun, Design of self-assembled nanoparticles as a potent inhibitor and fluorescent probe for β-amyloid fibrillization, *Langmuir*, 2023, **39**, 12576–12589; (*f*) A. Kour, T. Dube, A. Kumar and J. J. Panda, Anti-amyloidogenic and fibril disaggregating potency of the levodopa-functionalized gold nanoroses as exemplified in a diphenylalanine-based amyloid model, *Bioconjugate Chem.*, 2022, **33**, 397–410.

17 (*a*) F. Rofo, S. R. Meier, N. G. Metzendorf, J. I. Morrison, A. Petrovic, S. Syvänen, D. Sehlin and G. Hultqvist, A brain-targeting bispecific-multivalent antibody clears soluble amyloid-beta aggregates in Alzheimer's disease mice, *Neurotherapeutics*, 2022, **19**, 1588–1602; (*b*) F. Rofo, J. Buijs, R. Falk, K. Honek, L. Lannfelt, A. M. Lilja, N. G. Metzendorf, T. Gustavsson, D. Sehlin, L. Söderberg and G. Hultqvist, Novel multivalent design of a monoclonal antibody improves binding strength to soluble aggregates of amyloid beta, *Transl. Neurodegener.*, 2021, **10**, 1–16; (*c*) F. A. Aprile, P. Sormanni, M. Podpolny, S. Chhangur, L. M. Needham, F. S. Ruggeri, M. Perni, R. Limbocker, G. T. Heller, T. Sneideris and T. Scheidt, Rational design of a conformation-specific antibody for the quantification of Aβ oligomers, *Proc. Natl. Acad. Sci. U. S. A.*, 2020, **117**, 13509–13518.

18 (*a*) A. Dabas and B. Goyal, Structural reorganization mechanism of the $A\beta_{42}$ fibril mediated by N-substituted oligopyrrolamide ADH-353, *ACS Chem. Neurosci.*, 2024, **15**, 3136–3151; (*b*) M. Devi and S. Paul, Comprehending the efficacy of Whitlock's caffeine-pincered molecular tweezer on β-amyloid aggregation, *ACS Chem. Neurosci.*, 2024, **15**, 3202–3219; (*c*) S. S. Zhang, X. K. Yan, K. Feng, Y. J. Lao and

Y. R. Bao, Molecular insights into the structure destabilization effects of ECG and EC on the Aβ protofilament: An all-atom molecular dynamics simulation study, *Int. J. Biol. Macromol.*, 2023, **253**, 127002; (*d*) H. Okumura, Perspective for molecular dynamics simulation studies of amyloid-β aggregates, *J. Phys. Chem. B*, 2023, **127**, 10931–10940; Y. L. Han, H. H. Yin, C. Xiao, M. T. Bernards, Y. He and Y. X. Guan, Understanding the molecular mechanisms of polyphenol inhibition of amyloid β aggregation, *ACS Chem. Neurosci.*, 2023, **14**, 4051–4061; (*e*) A. Pasieka, D. Panek, N. Szałaj, A. Espargaró, A. Więckowska, B. Malawska, R. Sabaté and M. Bajda, Dual inhibitors of amyloid-β and tau aggregation with amyloid-β disaggregating properties: Extended in cellulo, *in silico*, and kinetic studies of multifunctional anti-Alzheimer's agents, *ACS Chem. Neurosci.*, 2021, **12**, 2057–2068; (*f*) Y. Wang, D. C. Latshaw and C. K. Hall, Aggregation of Aβ(17–36) in the presence of naturally occurring phenolic inhibitors using coarse–grained simulations, *J. Mol. Biol.*, 2017, **429**, 3893–3908; (*g*) Q. Wang, X. Yu, K. Patal, R. Hu, S. Chuang, G. Zhang and J. Zheng, Tanshinones inhibit amyloid aggregation by amyloid–β peptide, disaggregate amyloid fibrils, and protect cultured cells, *ACS Chem. Neurosci.*, 2013, **4**, 1004–1015.

19 (*a*) E. Gazit, A possible role for pi-stacking in the self-assembly of amyloid fibrils, *FASEB J.*, 2022, **16**, 77–83; (*b*) K. M. Makwana and R. Mahalakshmi, Implications of aromatic-aromatic interactions: From protein structures to peptide models, *Protein Sci.*, 2015, **24**, 1920–1933; (*c*) S. M. Tracz, A. Abedini, M. Driscoll and D. P. Raleigh, Role of aromatic interactions in amyloid formation by peptides derived from human Amylin, *Biochemistry*, 2004, **43**, 15901–15908.

20 (*a*) S. D. Shinde, S. K. Behera, N. Kulkarni, B. Dewangan and B. Sahu, Bifunctional backbone modified squaramide dipeptides as amyloid beta (Aβ) aggregation inhibitors, *Bioorg. Med. Chem.*, 2024, **97**, 117538; (*b*) A. Paul, G. K. Viswanathan, S. Mahapatra, G. Balboni, S. Pacifico, E. Gazit and D. Segal, Antagonistic activity of naphthoquinone-based hybrids toward amyloids associated with alzheimer's disease and type-2 diabetes, *ACS Chem. Neurosci.*, 2019, **10**, 3510–3520; (*c*) G. K. Viswanathan, A. Paul, E. Gazit and D. Segal, Naphthoquinone tryptophan hybrids: A promising small molecule scaffold for mitigating aggregation of amyloidogenic proteins and peptides, *Front. Cell Dev. Biol.*, 2019, **7**, 242; (*d*) R. Scherzer-Attali, R. Pellarin, M. Convertino, A. Frydman-Marom, N. Egoz-Matia, S. Peled, M. Levy-Sakin, D. E. Shalev, A. Caflisch, E. Gazit and D. Segal, Complete phenotypic recovery of an Alzheimer's disease model by a quinone-tryptophan hybrid aggregation inhibitor, *PLoS One*, 2010, **5**, e11101.

21 A. A. Mohammed, S. S. Barale, S. A. Kamble, S. B. Paymal and K. D. Sonawane, Molecular insights into the inhibition of early stage of Aβ peptide aggregation and destabilization of Alzheimer's Aβ protofibril by dipeptide D-Trp-Aib: A molecular modelling approach, *Int. J. Biol. Macromol.*, 2023, **242**, 124880.

22 V. G. KrishnaKumar, A. Paul, E. Gazit and D. Segal, Mechanistic insights into remodeled tau-derived PHF6 peptide fibrils by naphthoquinone-tryptophan hybrids, *Sci. Rep.*, 2018, **8**, 71.

23 S. V. Moradi, W. M. Hussein, P. Varamini, P. Simerska and I. Toth, Glycosylation, an effective synthetic strategy to improve the bioavailability of therapeutic peptides, *Chem. Sci.*, 2016, **7**, 2492–2500.

24 (*a*) A. Jain, A. Jain, P. Parajuli, V. Mishra, G. Ghoshal, B. Singh, U. S. Shivhare, O. P. Katare and P. Kesharwani, Recent advances in galactose-engineered nanocarriers for the site-specific delivery of siRNA and anticancer drugs, *Drug Discov. Today*, 2018, **23**, 960–973; (*b*) L. Feng, H. Yu, Y. Liu, X. Hu, J. Li, A. Xie, J. Zhang and W. Dong, Construction of efficacious hepatoma-targeted nanomicelles noncovalently functionalized with galactose for drug delivery, *Polym. Chem.*, 2014, **5**, 7121–7130; (*c*) Y. Wang, C.-Y. Hong and C.-Y. Pan, Galactose-based amphiphilic block copolymers: Synthesis, micellization, and bioapplication, *Biomacromolecules*, 2013, **14**, 1444–1451.

25 (*a*) T. D. Sandahl, J. A. E. Björklund, T. L. Laursen, P. Ott and H. Grønbæk, The galactose elimination capacity test may monitor treatment response and disease progression in patients with Wilson Disease, *J. Hepatol.*, 2018, **68**, S631; (*b*) S. Demirel, C. Argo, A. Agarwal, J. Parriott, Y. J. Sepah, D. V. Do and Q. D. Nguyen, Updates on the clinical trials in diabetic macular edema, *Middle East Afr. J. Ophthalmol.*, 2016, **23**, 3–12; (*c*) M. R. D. Cardoso, C. M. Mota, D. P. Ribeiro, P. G. Noleto, W. B. F. Andrade, M. A. Souza, N. M. Silva, T. W. P. Mineo, J. R. Mineo and D. A. O. Silva, Adjuvant and immunostimulatory effects of a D-galactose-binding lectin from Synadenium carinatum latex (ScLL) in the mouse model of vaccination against neosporosis, *Vet. Res.*, 2012, **43**, 76.

26 W. M. Pardridge and W. H. Oldendorf, Kinetics of blood-brain barrier transport of hexoses, *Biochim. Biophys. Acta, Biomembr.*, 1975, **382**, 377–392.

27 (*a*) S. S. Yuan, M. L. Li, J. S. Chen, L. Zhou and W. Zhou, Application of mono and disaccharides in drug targeting and efficacy, *ChemMedChem*, 2018, **13**, 764–778; (*b*) L. A. Ruocco, D. Viggiano, A. Viggiano, E. Abignente, M. G. Rimoli, D. Melisi, A. Curcio, M. Nieddu, G. Boatto, E. Carboni, U. A. Gironi Carnevale and A. G. Sadile, Galactosylated dopamine enters into the brain, blocks the mesocorticolimbic system and modulates activity and scanning time in Naples high excitability rats, *Neuroscience*, 2008, **152**, 234–244; (*c*) C. Fernández, O. Nieto, E. Rivas, G. Montenegro, J. A. Fontenla and A. Fernández-Mayoralas, Synthesis and biological studies of glycosyl dopamine derivatives as potential antiparkinsonian agents, *Carbohydr. Res.*, 2000, **327**, 353–365.

28 P. De Bona, M. Laura Giuffrida, F. Caraci, A. Copani, B. Pignataro, F. Attanasio, S. Cataldo, G. Pappalardo and E. Rizzarelli, Design and synthesis of new trehalose-conjugated pentapeptides as inhibitors of Aβ (1–42) fibrillogenesis and toxicity, *J. Pept. Sci.*, 2009, **15**, 220–228.

29 A. Paul, W. H. Li, G. K. Viswanathan, E. Arad, S. Mohapatra, G. Li, R. Jelinek, E. Gazit, Y. M. Li and D. Segal, Tryptophan–glucosamine conjugates modulate tau-derived PHF6 aggregation at low concentrations, *Chem. Commun.*, 2019, **55**, 14621–14624.

30 M. Frenkel-Pinter, M. Richman, A. Belostozky, A. Abu-Mokh, E. Gazit, S. Rahimipour and D. Segal, Selective inhibition of aggregation and toxicity of a tau-derived peptide using its glycosylated analogues, *Chem. – Eur. J.*, 2016, **22**, 5945–5952.

31 A. Paul, M. Frenkel–Pinter, D. Escobar Alvarez, G. Milordini, E. Gazit, E. Zacco and D. Segal, Tryptophan–galactosylamine conjugates inhibit and disaggregate amyloid fibrils of Aβ42 and hIAPP peptides while reducing their toxicity, *Commun. Biol.*, 2020, **3**, 484–496.

32 C. Zhan, Y. Chen, Y. Tang and G. Wei, Green tea extracts EGCG and EGC display distinct mechanisms in disrupting $A\beta_{42}$ protofibril, *ACS Chem. Neurosci.*, 2020, **11**, 1841–1851.

33 Y. Xiao, B. Ma, D. McElheny, S. Parthasarathy, F. Long, M. Hoshi, R. Nussinov and Y. Ishii, Aβ (1-42) fibril structure illuminates self-recognition and replication of amyloid in Alzheimer's disease, *Nat. Struct. Mol. Biol.*, 2015, **22**, 499–505.

34 T. Luhrs, C. Ritter, M. Adrian, D. Riek-Loher, B. Bohrmann, H. Dobeli, D. Schubert and R. Riek, 3D structure of Alzheimer's amyloid-β (1-42) fibrils, *Proc. Natl. Acad. Sci. U. S. A.*, 2005, **102**, 17342–17347.

35 A. K. Paravastu, R. D. Leapman, W. M. Yau and R. Tycko, Molecular structural basis for polymorphism in Alzheimer's β-amyloid fibrils, *Proc. Natl. Acad. Sci. U. S. A.*, 2008, **105**, 18349–18354.

36 M. Schmidt, A. Rohou, K. Lasker, J. K. Yadav, C. SchieneFischer, M. Fandrich and N. Grigorieff, Peptide dimer structure in an Aβ (1-42) fibril visualized with cryo-EM, *Proc. Natl. Acad. Sci. U. S. A.*, 2015, **112**, 11858–11863.

37 N. Mills, ChemDraw Ultra 10.0, *J. Am. Chem. Soc.*, 2006, **128**, 13649–13650.

38 J. M. Frisch, W. G. Trucks, B. H. Schlegel, E. G. Scuseria, A. M. Robb, R. J. Cheeseman, G. Scalmani, V. Barone, B. Mennucci, G. A. Petersson, H. Nakatsuji, M. Caricato, X. Li, H. P. Hratchian, A. F. Izmaylov, J. Bloino, G. Zheng, J. L. Sonnenberg, M. Hada, M. Ehara, K. Toyota, R. Fukuda, J. Hasegawa, M. Ishida, T. Nakajima, Y. Honda, O. Kitao, H. Nakai, T. Vreven, J. A. Montgomery, J. E. Peralta, F. Ogliaro, M. Bearpark, J. J. Heyd, E. Brothers, K. N. Kudin, V. N. Staroverov, R. Kobayashi, J. Normand, K. Raghavachari, A. Rendell, J. C. Burant, S. S. Iyengar, J. Tomasi, M. Cossi, N. Rega, J. M. Millam, M. Klene, J. Knox, J. B. Cross, V. Bakken, C. Adamo, J. Jaramillo, R. Gomperts, R. E. Stratmann, O. Yazyev, A. J. Austin, R. Cammi, C. Pomelli, J. W. Ochterski, R. L. Martin, K. Morokuma, V. G. Zakrzewski, G. A. Voth, P. Salvador, J. J. Dannenberg, S. Dapprich, A. D. Daniels, O. Farkas, J. B. Foresman, J. V. Ortiz, J. Cioslowski and D. J. Fox, *Gaussian 09, Revision E.01*, Gaussian, Inc., Wallingford, CT, 2009.

39 (*a*) M. Fang, Q. Zhang, P. Guan, K. Su, X. Wang and X. Hu, Insights into molecular mechanisms of EGCG and apigenin on disrupting amyloid-beta protofibrils based on molecular dynamics simulations, *J. Phys. Chem. B*, 2022, **126**, 8155–8165; (*b*) M. Fang, Q. Zhang, X. Wang, K. Su, P. Guan and X. Hu, Inhibition mechanisms of (−)-Epigallocatechin-3-gallate and Genistein on amyloid-beta 42 peptide of Alzheimer's disease via molecular simulations, *ACS Omega*, 2022, **7**, 19665–19675; (*c*) F. Li, C. Zhan, X. Dong and G. Wei, Molecular mechanisms of resveratrol and EGCG in the inhibition of $A\beta_{42}$ aggregation and disruption of $A\beta_{42}$ protofibril: similarities and differences, *Phys. Chem. Chem. Phys.*, 2021, **23**, 18843–18854.

40 K. Lindorff-Larsen, S. Piana, K. Palmo, P. Maragakis, J. L. Klepeis, R. O. Dror and D. E. Shaw, Improved side-chain torsion potentials for the Amber ff99SB protein force field, *Proteins: Struct., Funct., Bioinf.*, 2010, **78**, 1950–1958.

41 K. A. Malde, L. Zuo, M. Breeze, M. Stroet, D. Poger, C. P. Nair, C. Oostenbrink and E. A. Mark, An Automated Force Field Topology Builder (ATB) and repository: Version 1.0, *J. Chem. Theory Comput.*, 2011, **7**, 4026–4037.

42 (*a*) Y. Q. Huo, B. Yu, C. J. Liu, R. Zhou, H. H. Bao and S. W. Tang, Molecular insights into the inhibitory mechanisms of gallate moiety on the $A\beta_{1-40}$ amyloid aggregation: A molecular dynamics simulation study, *Int. J. Biol. Macromol.*, 2020, **156**, 40–50; (*b*) S. Hilt, T. Rojalin, T. Viitala, A. Koivuniemi, A. Bunker, S. Wachsmann-Hogiu, T. Kálai, K. Hideg, M. Yliperttula and J. C. Voss, Oligomerization alters binding affinity between amyloid beta and a modulator of peptide aggregation, *J. Phys. Chem. C*, 2017, **121**, 23974–23987.

43 O. Trott and A. J. Olson, AutoDock Vina: Improving the speed and accuracy of dockingwith a new scoring function, efficient optimization and multithreading, *J. Comput. Chem.*, 2010, **31**, 455–461.

44 (*a*) G. Bitencourt-Ferreira and W. F. de Azevedo Jr., Molegro virtual docker for docking, *Methods Mol. Biol.*, 2019, **2053**, 149–167; (*b*) R. Thomsen and M. H. Christensen, MolDock: A new technique for high-accuracy molecular docking, *J. Med. Chem.*, 2006, **49**, 3315–3321.

45 G. M. Morris, R. Huey, W. Lindstrom, M. F. Sanner, R. K. Belew, D. S. Goodsell and A. J. Olson, Autodock4 and AutoDockTools4: Automated docking with selective receptorflexiblity, *J. Comput. Chem.*, 2009, **16**, 2785–2791.

46 G. M. Morris, D. S. Goodsell, R. S. Halliday, R. Huey, W. E. Hart, R. K. Belew and A. J. Olson, Automated docking using a Lamarckian Genetic Algorithm and an empirical binding free energy function, *J. Comput. Chem.*, 1998, **19**, 1639–1662.

47 (*a*) R. Huey, G. M. Morris, A. J. Olson and D. S. Goodsell, A semiempirical free energy force field with charge-based desolvation, *J. Comput. Chem.*, 2007, **28**, 1145–1152; (*b*) J. F. Solis and J.-B. R. Wets, Minimization by random search techniques, *Math. Oper. Res.*, 1981, **6**, 19–30.

48 (*a*) R. A. Laskowski and M. B. Swindells, LigPlot+: Multiple ligand-protein interaction diagrams for drug discovery, *J. Chem. Inf. Model.*, 2011, **51**, 2778–2786; (*b*) W. L. DeLano, *The PyMOL molecular graphics system*, DeLano Scientific, San Carlos, CA, 2002, vol. 571.

49 M. J. Abraham, T. Murtola, R. Schulz, S. Pall, J. C. Smith, B. Hess and E. Lindahl, GROMACS: High performance molecular simulations through multi-level parallelism fromlaptops to supercomputers, *SoftwareX*, 2015, **1–2**, 19–25.

50 (*a*) M. Fang, X. Wang, K. Su, X. Jia, P. Guan and X. Hu, Inhibition effect and molecular mechanisms of quercetin on the Aβ42 dimer: A molecular dynamics simulation study, *ACS Omega*, 2023, **8**, 18009–18018; (*b*) D. Gao, J. Wan, Y. Zou, Y. Gong, X. Dong, Z. Xu, J. Tang, G. Wei and Q. Zhang, The destructive mechanism of $A\beta_{1-42}$ protofibrils by norepinephrine revealed via molecular dynamics simulations, *Phys. Chem. Chem. Phys.*, 2022, **24**, 19827–19836; (*c*) Z. Xu, Y. Gong, Y. Zou, J. Wan, J. Tang, C. Zhan, G. Wei and Q. Zhang, Dissecting the inhibitory mechanism of the αB-Crystallin domain against $A\beta_{42}$ aggregation and its effect on $A\beta_{42}$ protofibrils: a molecular dynamics simulation study, *ACS Chem. Neurosci.*, 2022, **13**, 2842–2851; (*d*) Y. Zou, Z. Qian, Y. Chen, H. Qian, G. Wei and Q. Zhang, Norepinephrine inhibits Alzheimer's amyloid-β peptide aggregation and destabilizes amyloid-β protofibrils: A molecular dynamics simulation study, *ACS Chem. Neurosci.*, 2019, **10**, 1585–1594.

51 (*a*) H. Bhagavatula, A. Sarkar, B. Santra and A. Das, Scan-find-scan-model: Discrete site targeted suppressor design strategy for amyloid–β, *ACS Chem. Neurosci.*, 2022, **13**, 2191–2208; (*b*) K. Singh, A. Kaur, D. Goyal and B. Goyal, Mechanistic insights into the mitigation of Aβ aggregation and protofibril destabilization by D–enantiomeric decapeptide rk10, *Phys. Chem. Chem. Phys.*, 2022, **24**, 21975–21994; (*c*) C. Zhan, Z. Lao, Y. Tang, Q. Qiao and G. Wei, Natural stereoisomeric flavonoids exhibit different disruptive effects and the mechanism of action on $A\beta_{42}$ protofibril, *Chem. Commun.*, 2021, **57**, 4267–4270; (*d*) P. Khatua, A. K. Jana and U. H. E. Hansmann, Effect of lauric acid on the stability of $A\beta_{42}$ oligomers, *ACS Omega*, 2021, **6**, 5795–5804.

52 (*a*) Z. Steinczinger, P. Jóvári and L. Pusztai, Comparison of 9 classical interaction potentials of liquid water: Simultaneous reverse Monte Carlo modeling of X-Ray and neutron diffraction results and partial radial distribution functions from computer simulations, *J. Mol. Liq.*, 2017, **228**, 19–24; (*b*) P. Mark and L. Nilsson, Structure and dynamics of the TIP3P, SPC, and SPC/E water models at 298 K, *J. Phys. Chem. A*, 2001, **105**, 9954–9960; (*c*) W. L. Jorgensen, J. Chandrasekhar, J. D. Madura, R. W. Impey and M. L. Klein, Comparison of simple potential functions for simulating liquid water, *J. Chem. Phys.*, 1983, **79**, 926–935.

53 A. M. Brown and D. R. Bevan, Molecular dynamics simulations of amyloid β-peptide (1–42): Tetramer formation and membrane interactions, *Biophys. J.*, 2016, **111**, 937–949.

54 G. Bussi, D. Donadio and M. Parrinello, Canonical sampling through velocity rescaling, *J. Chem. Phys.*, 2007, **126**, 014101–014109.

55 M. Parrinello and A. Rahman, Polymorphic transitions in single crystals: A new moleculardynamics method, *J. Appl. Phys.*, 1981, **52**, 7182–7190.

56 (*a*) U. Essmann, L. Perera, M. L. Berkowitz, T. Darden, H. Lee and L. G. Pedersen, Asmooth particle mesh Ewald method, *J. Chem. Phys.*, 1995, **103**, 8577–8593; (*b*) T. Darden, D. York and L. Pedersen, Particle mesh Ewald: An N·log (N) method for Ewald sums inlarge systems, *J. Chem. Phys*, 1993, **98**, 10089–10092.

57 B. Hess, H. Bekker, H. J. C. Berendsen and J. G. E. M. Fraaije, LINCS: A linear constraintsolver for molecular simulations, *J. Comput. Chem.*, 1997, **18**, 1463–1472.

58 S. Miyamoto and P. A. Kollman, Settle: An analytical version of the SHAKE and RATTLEalgorithm for rigid water models, *J. Comput. Chem.*, 1992, **13**, 952–962.

59 (*a*) L. J. Smith, X. Daura and W. F. van Gunsteren, Assessing equilibration and convergencein biomolecular simulations, *Protein Struct. Funct. Bioinf.*, 2002, **48**, 487–496; (*b*) X. Daura, K. Gademann, B. Jaun, D. Seebach, W. F. van Gunsteren and A. E. Mark, Peptide folding:When simulation meets experiment, *Angew. Chem., Int. Ed.*, 1999, **38**, 236–240.

60 S. K. Burley and G. A. Petsko, Aromatic-aromatic interaction: A mechanism of protein structure stabilization, *Science*, 1985, **229**, 23–28.

61 Y. Chen, X. Li, C. Zhan, Z. Lao, F. Li, X. Dong and G. Wei, A comprehensive insight into the mechanisms of dopamine in disrupting Aβ protofibrils and inhibiting Aβ aggregation, *ACS Chem. Neurosci.*, 2021, **12**, 4007–4019.

62 R. Kumari and R. Kumar, g_mmpbsa—A GROMACS tool for high-throughput MM-PBSAcalculations, *J. Chem. Inf. Model.*, 2014, **54**, 1951–1962.

63 (*a*) L. Xie, Y. Luo, D. Lin, W. Xi, X. Yang and G. Wei, The molecular mechanism of fullerene-inhibited aggregation of Alzheimer's β-amyloid peptide fragment, *Nanoscale*, 2014, **6**, 9752–9762; (*b*) T. Zhang, W. Xu, Y. Mu and P. Derreumaux, Atomic and dynamic insights into the beneficial effect of the 1, 4-naphthoquinon-2-yl-l-tryptophan inhibitor on Alzheimer's Aβ1–42 dimer in terms of aggregation and toxicity, *ACS Chem. Neurosci.*, 2014, **5**, 148–159; (*c*) T. Zhang, J. Zhang, P. Derreumaux and Y. Mu, Molecular mechanism of the inhibition of EGCG on the Alzheimer Aβ1–42 dimer, *J. Phys. Chem. B*, 2013, **117**, 3993–4002; (*d*) P. A. Novick, D. H. Lopes, K. M. Branson, A. Esteras-Chopo, I. A. Graef, G. Bitan and V. S. Pande, Design of β-amyloid aggregation inhibitors from a predicted structural motif, *J. Med. Chem.*, 2012, **55**, 3002–3010; (*e*) R. B. Best, N. V. Buchete and G. Hummer, Are current molecular dynamics force fields too helical?, *Biophys. J.*, 2008, **9**, L07–L09.

64 (*a*) B. Han, Y. Liu, W. S. Ginzinger and S. D. Wishart, SHIFTX2: Significantly improvedprotein chemical shift prediction, *J. Biomol. NMR*, 2011, **50**, 43–57; (*b*) S. Neal, A. M. Nip, H. Zhang and D. S. Wishart, Rapid and accurate calculation of protein ^{1}H, ^{13}C and ^{15}Nchemical shifts, *J. Biomol. NMR*, 2003, **26**, 215–240.

65 **https://bmrb.io/data_library/summary/?bmrbId=27212**, DOI: **10.13018/BMR27212**.

66 Y. Shen and A. Bax, Protein structural information derived from NMR chemical shift with the neural network program TALOS-N, *Methods Mol. Biol.*, 2015, **1260**, 17–32.

67 M. Karplus, Contact electron–spin coupling of nuclear magnetic moments, *J. Chem. Phys.*, 1959, **30**, 11–15.
68 H. Tian, R. Ketkar and P. Tao, ADMETboost: a web server for accurate ADMET prediction, *J. Mol. Model.*, 2022, **28**, 408.
69 G. Xiong, Z. Wu, J. Yi, L. Fu, Z. Yang, C. Hsieh, M. Yin, X. Zeng, C. Wu, A. Lu and X. Chen, ADMETlab 2.0: An integrated online platform for accurate and comprehensive predictions of ADMET properties, *Nucleic Acids Res.*, 2021, **49**, W5–W14.
70 (*a*) C. Sackmann and M. Hallbeck, Oligomeric amyloid−β induces early and widespread changes to the proteome in human iPSC-derived neurons, *Sci. Rep.*, 2020, **10**, 6538–6550; (*b*) E. N. Cline, M. A. Bicca, K. L. Viola and W. L. Klein, The amyloid-oligomer hypothesis: Beginning of the third decade, *J. Alzheimer's Dis.*, 2018, **64**, S567–S610; (*c*) U. Sengupta, A. N. Nilson and R. Kayed, The role of amyloid−β oligomers in toxicity, propagation, and immunotherapy, *eBioMedicine*, 2016, **6**, 42–49.
71 R. Mallesh, J. Khan, K. Pradhan, R. Roy, N. R. Jana, P. Jaisankar and S. Ghosh, Design and development of benzothiazole-based fluorescent probes for selective detection of Aβ aggregates in Alzheimer's disease, *ACS Chem. Neurosci.*, 2022, **13**, 2503–2516.
72 S. Xu, Y. Sun and X. Dong, Design of gallic acid–glutamine conjugate and chemicalimplications for its potency against Alzheimer's amyloid–β fibrillogenesis, *Bioconjugate Chem.*, 2022, **33**, 677–690.
73 Y. Gong, C. Zhan, Y. Zou, Z. Qian, G. Wei and Q. Zhang, Serotonin and melatonin show different modes of action on $A\beta_{42}$ protofibril destabilization, *ACS Chem. Neurosci.*, 2021, **12**, 799–809.
74 M. Fang, K. Su, X. Wang, P. Guan and X. Hu, Study on molecular mechanisms of destabilizing Aβ(1–42) protofibrils by licochalcone A and licochalcone B using molecular dynamics simulations, *J. Mol. Graphics Modell.*, 2023, **122**, 108500.
75 D. S. Knopman, H. Amieva, R. C. Petersen, G. Chetelat, D. M. Holtzman, B. T. Hyman, R. A. Nixon and D. T. Jones, Alzheimer disease, *Nat. Rev. Dis. Prim.*, 2021, **7**, 33.
76 C. A. Söldner, H. Sticht and A. H. Horn, Role of the N-terminus for the stability of an amyloid-β fibril with three-fold symmetry, *PLoS One*, 2017, **12**, 0186347.
77 (*a*) S. Kaumbekova, M. A. Torkmahalleh and D. Shah, Ambient benzo[a]pyrene's effect on kinetic modulation of amyloid beta peptide aggregation: A tentative association between ultrafine particulate matter and Alzheimer's disease, *Toxics*, 2022, **10**, 786; (*b*) N. T. Tung, P. Derreumaux, V. V. Vu, P. C. Nam and S. T. Ngo, C-terminal plays as the possible nucleation of the self-aggregation of the S-shape $A\beta_{11-42}$ tetramer in solution: Intensive MD study, *ACS Omega*, 2019, **4**, 11066–11073.
78 I. M. Stanković, D. M. Bozinovski, E. N. Brothers, M. R. Belić, M. B. Hall and S. D. Zarić, Interactions of aromatic residues in amyloids: A survey of protein data bank crystallographic data, *Cryst. Growth Des.*, 2017, **17**, 6353–6362.
79 (*a*) J. Kumar, R. Namsechi and V. L. Sim, Structure-based peptide design to modulate amyloid beta aggregation and reduce cytotoxicity, *PLoS One*, 2015, **10**, e0129087; (*b*) H. Inouye, K. A. Gleason, D. Zhang, S. M. Decatur and D. A. Kirschner, Differential effects of Phe19 and Phe20 on fibril formation by amyloidogenic peptide Aβ16–22 (Ac–KLVFFAE–NH_2), *Proteins: Struct., Funct., Bioinf.*, 2010, **78**, 2306–2321.
80 Y. P. Singh, N. Kumar, K. Priya, B. S. Chauhan, G. Shankar, S. Kumar, G. K. Singh, S. Srikrishna, P. Garg, G. Singh and G. Rai, Exploration of neuroprotective properties of a naturally inspired multifunctional molecule (F24) against oxidative stress and amyloid β induced neurotoxicity in Alzheimer's disease models, *ACS Chem. Neurosci.*, 2022, **13**, 27–42.
81 M. A. Wälti, F. Ravotti, H. Arai, C. G. Glabe, J. S. Wall, A. Böckmann, P. Güntert, B. H. Meier and R. Riek, Atomic-resolution structure of a disease-relevant Aβ (1–42) amyloid fibril, *Proc. Natl. Acad. Sci. U. S. A.*, 2016, **113**, E4976–E4984.
82 (*a*) D. de Raffele and I. M. Ilie, Unlocking novel therapies: Cyclic peptide design for amyloidogenic targets through synergies of experiments, simulations, and machine learning, *Chem. Commun.*, 2024, **60**, 632–645; (*b*) A. Thomas, G. Kaur, R. Ali and S. Verma, in Small molecule inhibitors for amyloid aggregation, eds: C. Nardin and H. Schlaad, *Biological Soft Matter: Fundamentals, Properties, and Applications*, Wiley-Vch GmbH, 2021; (*c*) A. J. Doig and P. Derreumaux, Inhibition of protein aggregation and amyloid formation by small molecules, *Curr. Opin. Struct. Biol.*, 2015, **30**, 50–56; (*d*) J. A. Lemkul and D. R. Bevan, The role of molecular simulations in the development of inhibitors of amyloid β-peptide aggregation for the treatment of Alzheimer's disease, *ACS Chem. Neurosci.*, 2012, **3**, 845–856.